Glycerol-assisted co-electrolysis in solid oxide electrolyzer cell (SOEC) for green syngas production: a 2D modelling study

Chen Wang[1], Zheng Li[1], Daqin Guan[1], Meng Zhu[1], Idris Temitope Bello[1], Minfang Han[2,*], Meng Ni[1,*]

[1] Department of Building and Real Estate, Research Institute for Sustainable Urban Development (RISUD) and Research Institute for Smart Energy (RISE), The Hong Kong Polytechnic University, Hung Hom, Kowloon, Hong Kong, China

[2] Department of Energy and Power Engineering, Tsinghua University, Beijing, 100084, China

* Corresponding author:

Email: meng.ni@polyu.edu.hk (Meng Ni)

hanminfang@tsinghua.edu.cn (Minfang Han)

Abstract

A 2D multi-physics model is developed to study the glycerol-assisted SOEC co-electrolysis process, with a novel in-tube reformer to improve the fuel utilization and reduce the temperature difference. After model validation, the effects of key operating parameters on the electrochemical performance and temperature distribution of the system are investigated. It is found that glycerol assistance can significantly reduce the operating voltage of the SOEC co-electrolysis system, thus saving over 55% of electrical energy at 1073K. Besides, increasing operating voltage, operating temperature and cathode H_2O molar fraction promote the co-electrolysis process, leading to an increase in cathode H_2O/CO_2 conversion. Optimal values of the anode/cathode flow rates (Q_{an}=70~110 SCCM and Q_{ca}=125~175 SCCM) and the anode glycerol molar fraction ($X_{an,GL}$=0.05~0.15) are obtained to achieve both good electrochemical performance and uniform temperature distribution. Meanwhile, the proposed in-tube reformer can greatly reduce the temperature difference inside the cell, and by precisely controlling the structure and operating parameters of the system, a more uniform internal temperature distribution can be obtained, even allowing the system to be operated at homogeneous temperature conditions. This study provides a reference for the commercialization of efficient green syngas production and CO_2 recycling by using renewable electricity.

Keywords

Solid oxide electrolyzer cell; Numerical modeling; Fuel assisted co-electrolysis; CO_2 recycling; Thermal effect.

35 **Nomenclature**

36 Abbreviation

SOEC	Solid oxide electrolyzer cell
SOFEC	Solid oxide fuel-assisted electrolyzer cell
TPB	Triple phase boundary

37 Letter

R_i	Chemical reaction rate
E_{act}	Activation energy, J·mol^{-1}
E_{eq}	Equilibrium potential, V
ρ	Density, kg·m^{-3}
γ_i	Pre-exponential factor
σ	Conductivity, S·m^{-1}
T	Temperature, K
μ	Dynamic viscosity, kg·m^{-1}·s^{-1}
R	Universal gas constant, 8.314 J·mol^{-1}·K^{-1}
ε	Porosity
ϕ	Electrostatic potential, V
F	Faraday constant, 96485.3 C·mol^{-1}
k	Permeability, m^2
y_i	Molar fraction of specie i
λ_{eff}	Effective thermal conductivity, W·m^{-1}·K^{-1}
ΔH^0	Enthalpy change, J·mol^{-1}
ΔS^0	Entropy change, J·mol^{-1}·K^{-1}
f_i	Fugacity of specie i, Pa
$D_{ij,eff}$	Effective binary diffusion coefficient, m^2·s^{-1}
$D_{ik,eff}$	Effective Knudsen diffusion coefficient, m^2·s^{-1}
c_p	Specific heat capacity, J·mol^{-1}·K^{-1}
Q_i	Heat source term
τ	Tortuosity

1 Introduction

Renewable energy (e.g. wind, solar, tidal, etc.) plays an important role in achieving carbon neutrality and a low-carbon energy economy in the future [1]. For example, by 2050, the United States intends to expand its renewable electricity use to 80%, while the European Union aims to replace 55% of its electricity demand with renewable energy [2]. However, the high intermittency and severe environmental dependence of renewable energy limits its large-scale development, leading to an increasingly urgent need for efficient and cost-effective large-scale energy storage solutions [3-6].

Among various energy storage systems (e.g. pumped hydropower system, redox flow batteries, compressed air system, chemical energy storage, etc.), the conversion of renewable electricity to chemical energy in valuable chemicals through solid oxide electrolyzer cell (SOEC) is an extremely promising pathway [7,8]. SOEC operates under high temperature conditions, which can significantly reduce electrical energy consumption and has the advantage of high efficiency, material flexibility and reverse operation, compared to low temperature electrolysis systems [9,10]. However, although part of the electricity is replaced by thermal energy in SOEC operating at high temperatures, electrical energy is still the main energy consumption and accounts for the major cost (even larger than 70%) during the operation of the SOEC electrolysis system [11,12]. This is due to the fact that in SOEC, the anode is usually exposed to ambient air with high oxygen partial pressure, which creates a large oxygen partial pressure difference with the reducing atmosphere at the cathode side. Although the efficient catalyst or novel heterostructured electrodes can reduce the oxygen partial pressure difference by facilitating the oxygen evolution reaction (OER) reaction at anode [13,14], it still results in an open circuit voltage (OCV) of up to 1 V at typical operating temperatures (800 ℃), which consumes a large amount of electrical energy and reduces the electrolysis efficiency [15,16]. Consequently, the large electrical energy consumption makes the cost of electrolytic hydrogen

production 2-3 times higher than that of conventional hydrogen production by steam reforming of fossil fuels [15].

Solid oxide fuel-assisted electrolyzer cell (SOFEC) is a promising new electrolysis method that can reduce the O_2 partial pressure by rapidly consuming the oxygen produced at the anode, thus overcoming the large overpotential in the OER reaction and reducing the equilibrium potential of electrolysis [15]. According to statistics, more than 50% of the energy in water electrolysis can be provided by the chemical energy in hydrocarbons, thus greatly reducing the electrical energy consumption to 1/3 to 1/2 of that in the conventional electrolyzer cells [15,17,18]. And since the assisting fuels such as hydrocarbons are utilized directly by electrochemical process, which has a much higher efficiency than the Carnot cycle (utilized by combustion), therefore, it can reduce emissions and operate efficiently. Several studies have been conducted on the use of fuels such as carbon [18,19], CO [20], methane [21,22], and ethanol [23] to assist the electrolysis process in SOEC. Lei et al. [18] proposed a new high-efficiency syngas generator by combining carbon gasification and SOEC co-electrolysis, and found that the co-electrolysis potential can be reduced by 1 V, which can save more than 90% of the electrical energy input. Wang et al. [22] investigated the performance of methane-assisted SOEC co-electrolysis for syngas production and found that by replacing the anode atmosphere from air to methane, the Nernst potential could be reduced by an order of magnitude, achieving a current density of -242 $mA \cdot cm^{-2}$ at 850°C and 0.3 V. Liu et al. [23] developed a SOEC reactor for ethanol-assisted water electrolysis, enabling thermally neutral operation by integrating the fiber reactor in the anode channel, and achieving a stable operation at an ultra-high current density of 3 $A \cdot cm^{-2}$. However, the current modelling studies lack sufficient consideration of the thermal effects within the fuel-assisted SOEC.

Among various hydrocarbon fuels, glycerol is a byproduct of biodiesel and is a renewable chemical with high energy density, non-toxicity and chemical stability [24]. Glycerol has been

produced in large quantities (10% of biodiesel weight) as a byproduct due to the explosive growth of the biodiesel industry [25]. The international market for glycerol is predicted to reach $3.5 billion by 2027, and is growing at a compound annual growth rate (CAGR) of 4% [26]. However, as biodiesel production increases, an increasing amount of glycerol is being discarded, since only a small percentage is purified for further use [25]. Although several studies have been conducted on the use of glycerol for hydrogen production [27-30], the glycerol reforming reaction is highly heat-absorbing and requires a constant supply of heat from outside, which is a typical energy-intensive industry and does not meet the requirements of a low-carbon economy. Therefore, the use of glycerol to assist the electrolysis process in SOEC not only avoids the waste of glycerol, but also has a promising prospect of recycling CO_2 through electrolysis, reducing carbon emissions as well as providing green syngas (currently, syngas is mainly obtained through the reforming of fossil fuels [31]) for later Fischer-Tropsch synthesis [32]. Moreover, through the proper design of the internal reformer, it is possible to match the heat absorption of the glycerol reforming reaction with the exotherm of the electrochemical reaction, thus achieving the overall internal thermal neutrality and even eliminating the obvious temperature difference within the cell.

Despite these benefits, few studies on glycerol-assisted SOEC have been conducted. The mechanism of the co-electrolysis process within the glycerol-assisted SOEC system and the effect of key operating parameters on the assisted electrolysis process are still unknown. Therefore, a 2D multi-physics numerical model was developed to simulate the H_2O/CO_2 co-electrolysis process in a glycerol-assisted tubular SOEC in this study. A novel in-tube reformer is proposed to improve the fuel utilization efficiency and reduce the temperature difference within the cell. The model fully considers the flow, diffusion, chemical and electrochemical processes and thermal effects in the SOEC. The effects of key operating parameters (flow rate and inlet gas composition) and operating conditions (temperature and operating voltage) on the

glycerol-assisted co-electrolysis system are analyzed as well as providing the optimal operating conditions. This study provides an insight into the co-electrolysis process in glycerol-assisted SOEC, which can facilitate the CO_2 recovery and green syngas production by using renewable energy.

2 Modelling methodology

2.1 Physical model

Fig. 1(a) illustrates the system flow chart during operation and Fig. 1(b) demonstrates the scheme of the tubular glycerol-assisted co-electrolysis SOEC system. The system uses an anode-supported tubular SOEC for electrolysis, where the fuel (glycerol) used for electrolysis assistance is supplied to the cell using a stainless steel tube, and the cathode and anode channels are in a counter-flow arrangement. The cell uses YSZ (yttria-stabilized zirconia) as the electrolyte, the mixture of Ni-YSZ as the anode and cathode, with the thicknesses of 10μm, 600μm, and 100μm, respectively. In order to improve the glycerol conversion, an in-tube reformer is arranged inside the stainless steel tube, which is consisted of a 400μm porous medium with a homogenous distribution of the catalyst ($Ni\text{-}Al_2O_3$) for glycerol conversion. Due to the small size and strong entrance effect of the anode corner (the bottom of the tubular SOEC, served to conduct the gas mixture from the inner tube to the anode channel), only the fluid flow, species transfer and heat exchange in the anode corner are considered, without considering the chemical and electrochemical reactions in this region. The detailed geometric dimensions and material properties are shown in Table 1.

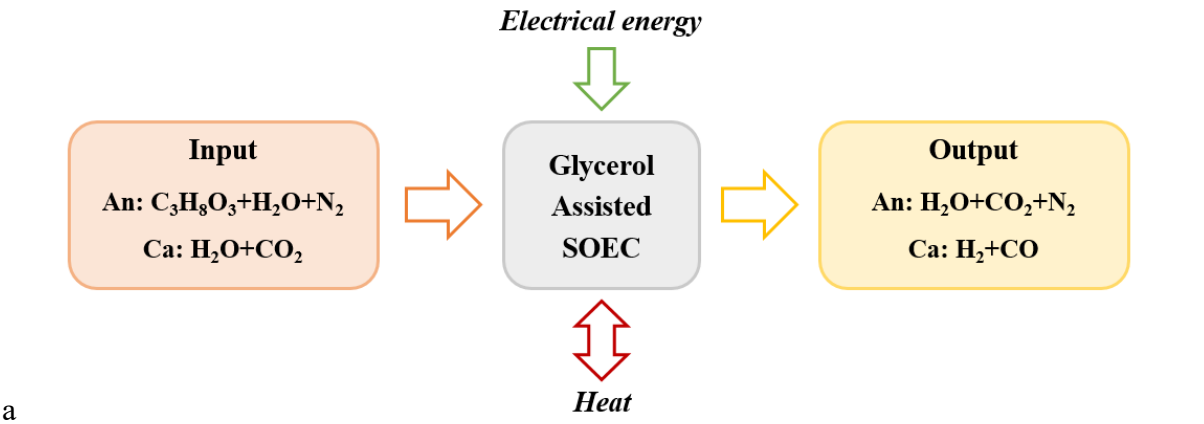

a

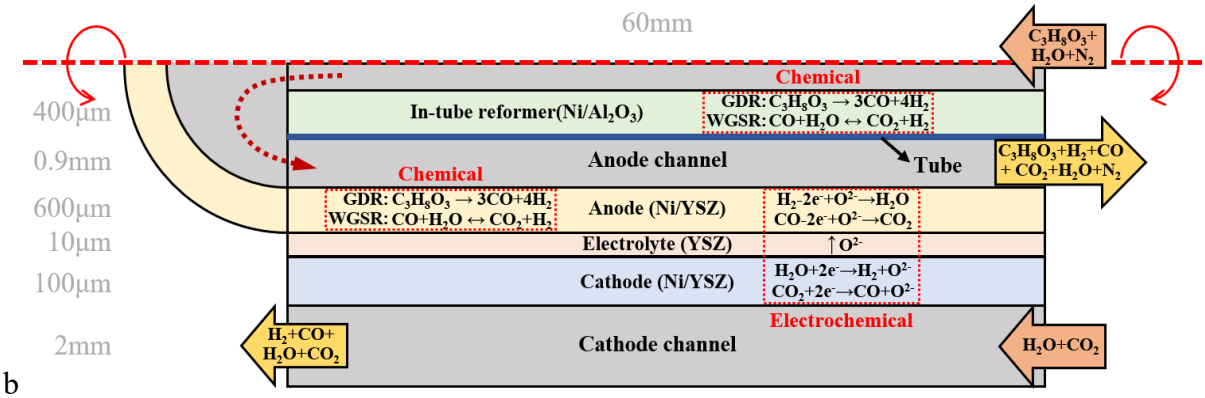

b

Fig.1 (a) System flow chart; (b) tubular glycerol-assisted co-electrolysis SOEC

Table 1 Geometric dimensions and material properties [33-36]

Materials or Parameters	Expression or Value	Unit
Conductivity		
Ni	3.27×10^{6}-1065.3×T	$S\cdot m^{-1}$
YSZ	$3.34\times10^{4}\times\exp(-10300\times T^{-1})$	$S\cdot m^{-1}$
Dimensions		
Length of cell	62.6	mm
Length of anode tube	60	mm
Inner/Outer radius of anode tube	1.0/1.1	mm
Inner/Outer radius of anode channel	1.1/2.0	mm
Inner/Outer radius of cathode channel	2.71/4.71	mm

Thickness of in-tube reformer	400	μm
Anode	600	μm
Cathode	100	μm
Electrolyte	10	μm
Tortuosity	3	-
Porosity		
Anode	0.4	-
Cathode	0.4	-
In-tube reformer	0.4	-
Permeability		
Anode	1.76×10^{-11}	m^2
Cathode	1.76×10^{-11}	m^2
In-tube reformer	1.76×10^{-11}	m^2
S_{TPB}		
Anode	3.33×10^{5}	$m^2\cdot m^{-3}$
Cathode	2.66×10^{5}	$m^2\cdot m^{-3}$
α		
α_{an}	0.5	-
α_{ca}	0.65	-
γ		
$\gamma_{an,H2}$	7×10^{8}	-
$\gamma_{ca,H2}$	1.5×10^{9}	-
E_{act}		
$E_{act,an}$	1.3×10^{5}	$J\cdot mol^{-1}$
$E_{act,ca}$	1.2×10^{5}	$J\cdot mol^{-1}$

During operation, the anode and cathode channels are using a counter-flow configuration. H_2O and CO_2 are supplied into the cathode channel, while glycerol and H_2O are supplied into the anode tube with some N_2 served as carrier gas. For the general co-electrolysis system without assisting, the H_2O and CO_2 are electrolyzed at the TPBs of cathode, gaining electrons, forming H_2 and CO, as well as releasing O^{2-} (Eqs. (1), (2)). Then, O^{2-} is transferred to the anode through the oxygen-ion conducting electrolyte and will release O_2 by losing electrons at the TPBs of anode (Eq. (3)), while the electrons will be delivered to the cathode through an external circuit to participate in the electrolysis process of H_2O and CO_2. However, for the glycerol assisted co-electrolysis system, although the co-electrolysis process of H_2O and CO_2 at the cathode is the same as the unassisted system (Eqs. (1), (2)), while at the anode, the glycerol supplied into the anode tube will be consumed through the glycerol steam reforming reaction (GSR, Eq. (4), which is composed of the glycerol deposition reaction (GDR, Eq. (5)) and water gas shift reaction (WGSR, Eq. (6))) catalyzed by Ni-based catalyst in the in-tube reformer and the anode electrode to produce H_2 and CO. Subsequently, the produced H_2 and CO will react directly with O^{2-} delivered from the cathode at the anode TPBs (Eqs. (7), (8)), releasing electrons and forming H_2O and CO_2, so as to assist the co-electrolysis process. Although methane may be formed on the Ni-based catalyst during operation (Eqs. (9), (10)), it requires low temperature and high pressure conditions [37], so methane formation is inhibited and not considered under the conditions of study. While carbon deposition may be caused through some side reactions (Eqs. (11), (12)), it was not obvious and performed a stable operation for 49 hours in the experiment [39], so carbon deposition is also not considered.

$$H_2O+2e^- \rightarrow H_2 + O^{2-} \quad (1)$$

$$CO_2+2e^- \rightarrow CO + O^{2-} \quad (2)$$

$$O^{2-}-2e^- \rightarrow 0.5O_2 \quad (3)$$

$$C_3H_8O_3 + 3H_2O \rightarrow 3CO_2+7H_2\ ,\ \Delta H_{298K} = 128 kJ/mol \quad (4)$$

$$C_3H_8O_3 \rightarrow 3CO+4H_2\ ,\ \Delta H_{298K} = 251kJ/mol \quad (5)$$

$$CO+H_2O \leftrightarrow CO_2+H_2\ ,\ \Delta H_{298K} = -41kJ/mol \quad (6)$$

$$H_2\text{-}2e^- + O^{2-} \rightarrow H_2O \quad (7)$$

$$CO\text{-}2e^- + O^{2-} \rightarrow CO_2 \quad (8)$$

$$CO+3H_2 \leftrightarrow CH_4+H_2O\ ,\ \Delta H_{298K} = -206kJ/mol \quad (9)$$

$$CO_2+4H_2 \leftrightarrow CH_4+2H_2O\ ,\ \Delta H_{298K} = -164kJ/mol \quad (10)$$

$$2CO(g) \leftrightarrow CO_2(g)+C(s)\ ,\ \Delta H_{298K} = -171kJ/mol \quad (11)$$

$$CO(g)+H_2(g) \leftrightarrow H_2O(g)+C(s)\ ,\ \Delta H_{298K} = -131kJ/mol \quad (12)$$

The following assumptions are adopted based on the above mechanisms in this study:

(1) The gases are incompressible and ideal.

(2) The active sites are homogeneous for the chemical/electrochemical reactions.

(3) Heat radiation, carbon deposition, and methane formation are not considered.

(4) Only H_2 and CO will react electrochemically.

(5) The electronic/ionic conducting phase is uniformly distributed and continuous.

2.2 Chemical model

In the in-tube reformer and the anode electrode, glycerol is converted to H_2 and CO through the glycerol steam reforming reaction (GSR, Eq. (4)), which is composed of the glycerol decomposition reaction (GDR, Eq. (5)) and water gas shift reaction (WGSR, Eq. (6)). While at the cathode electrode, the WGSR will occur apart from the electrolysis of H_2O/CO_2. In this study, the reaction rates of GDR and WGSR are described as:

GDR [40]:

$$R_{GDR} = 0.036e^{\frac{-63300}{RT}} p_{C_3H_8O_3}^{0.253} p_{H_2O}^{0.358} A_{\text{metal surface}} \quad (13)$$

WGSR [35]:

$$R_{\mathrm{WGSR}}=0.0171\mathrm{e}^{\frac{-103196}{RT}}\left(p_{\mathrm{H_2O}}p_{\mathrm{CO}}-\frac{p_{\mathrm{H_2}}p_{\mathrm{CO_2}}}{K_{ps}}\right) \quad (14)$$

$$K_{ps}=\exp(-0.2935Z^3+0.6351Z^2+4.1788Z+0.3169) \quad (15)$$

$$Z=\frac{1000}{T}-1 \quad (16)$$

where T is reacting temperature, K; R is gas constant, 8.314 J·mol^{-1}·K^{-1}; p_i is the partial pressure of specie i, Pa; $A_{\mathrm{metal\ surface}}$ is metal surface area of the catalyst, m^2.

2.3 Electrochemical model

During operation, H_2O and CO_2 are electrolyzed to produce H_2 and CO (Eqs. (1), (2)) at the cathode TPBs. The operating potential (V) in the electrolysis process is described as:

$$V=E+\eta_{\mathrm{act,an}}+\eta_{\mathrm{act,ca}}+\eta_{\mathrm{ohmic}} \quad (17)$$

where E is equilibrium potential, V; η_{act} is activation overpotential, V; η_{ohmic} is ohmic overpotential, V.

For the general co-electrolysis cell without assisting, E is calculated by using the Nernst equation [33,35]:

$$E_{\mathrm{H_2}}=E^0_{\mathrm{H_2}}+\frac{RT}{2F}\left(\frac{p_{\mathrm{H_2}}\left(p_{\mathrm{O_2}}\right)^{0.5}}{p_{\mathrm{H_2O}}}\right) \quad (18)$$

$$E_{\mathrm{CO}}=E^T_{\mathrm{CO}}+\frac{RT}{2F}\left(\frac{p_{\mathrm{CO}}\left(p_{\mathrm{O_2}}\right)^{0.5}}{p_{\mathrm{CO_2}}}\right) \quad (19)$$

$$E^0_{\mathrm{H_2}}=1.253-0.00024516T \quad (20)$$

$$E^T_{\mathrm{CO}}=1.46713-0.0004527T \quad (21)$$

where F is the Faraday constant; E^0_{H2} and E^0_{CO} are the standard cell potentials, V.

While for the glycerol assisted co-electrolysis cell, since O_2 is no longer a product in the anode, but instead H_2 and CO are directly oxidized by O^{2-} to form H_2O and CO_2. The model

based on the oxygen partial pressure is used to describe the equilibrium potential as [34,41]:

$$E_{\mathrm{OCV}} = \frac{RT}{nF}\ln\left(\frac{p_{\mathrm{O_2},ca}}{p_{\mathrm{O_2},an}}\right) \tag{22}$$

where n is the number of electrons transferred in the electrochemical reaction; $p_{O2,ca}$ and $p_{O2,an}$ are the oxygen partial pressures at the cathode and anode, respectively.

For the electrochemical reaction of H_2 and CO, the oxygen partial pressure can be further described as [34,41]:

$$p_{\mathrm{O_2},\mathrm{H_2/H_2O}} = \left(\frac{p_{\mathrm{H_2O}}}{p_{\mathrm{H_2}}}\cdot\exp\left(\frac{\Delta G_{\mathrm{H_2/H_2O}}}{RT}\right)\right)^2 \tag{23}$$

$$p_{\mathrm{O_2},\mathrm{CO/CO_2}} = \left(\frac{p_{\mathrm{CO_2}}}{p_{\mathrm{CO}}}\cdot\exp\left(\frac{\Delta G_{\mathrm{CO/CO_2}}}{RT}\right)\right)^2 \tag{24}$$

where ΔG represents the Gibbs free energy change during the electrochemical reaction, $J\cdot mol^{-1}$.

The Butler-Volmer (BV) equation is used to describe the relationship between current density and activation overpotential as [33,35]:

$$i = i_0\left[\exp\left(\frac{\alpha nF\eta_{act}}{RT}\right) - \exp\left(\frac{-(1-\alpha)nF\eta_{act}}{RT}\right)\right] \tag{25}$$

where i_0 is the exchange current density, $A\cdot m^{-2}$; α is the electron transfer coefficient; n is the number of electrons transferred per reaction.

The exchange current density for H_2/H_2O electrochemical reaction can be further expressed as [34,36]:

$$i_{0,an,H_2} = \gamma_{an,H_2}\cdot\exp\left(-\frac{E_{act,an}}{RT}\right) \tag{26}$$

$$i_{0,ca,H_2} = \gamma_{ca,H_2}\cdot pH_{2,ca}^{TPB}\cdot\exp\left(-\frac{E_{act,ca}}{RT}\right) \tag{27}$$

where $\gamma_{an,H2}$ and $\gamma_{ca,H2}$ represent the pre-expontential factors for the anode and cathode sides,

225 respectively; E_{act} is activation energy, J·mol^{-1}; $p_{H2,ca}^{TPB}$ is the partial pressure of H_2 at the cathode
226 TPBs, Pa.

227 For the CO/CO_2 electrochemical reaction, since the electrolysis rate of H_2O is
228 experimentally observed to be 2.2 times higher than the electrolysis of CO_2 [38], the exchange
229 current density of CO electrochemical reaction in this study is assumed as [34,38]:

230 $$i_{0,ca,CO} = \frac{1}{2.2} \cdot i_{0,ca,H_2} \tag{28}$$

231 Besides, the transport of oxygen-ions/electrons in the electrodes and electrolyte is described
232 by using the Ohm's law:

233 $$i_{oi} = -\sigma_{oi,eff} \nabla(Ø_{oi}) \tag{29}$$

234 $$i_{e} = -\sigma_{e,eff} \nabla(Ø_{e}) \tag{30}$$

235 where $Ø_{oi}$ and $Ø_e$ represent the conducting potentials of oxygen-ion and electron, respectively;
236 $\sigma_{oi,eff}$ and $\sigma_{e,eff}$ represent the effective conductivity of oxygen-ion phase and electron phase in
237 the porous electrodes, respectively. This is further calculated using tortuosity (τ) and volume
238 fractions of oxygen-ion (V_{oi}) phase and electron (V_e) phase in the electrodes as:

239 $$\sigma_{oi,eff} = \sigma_{oi} \frac{V_{oi}}{\tau_{oi}} \tag{31}$$

240 $$\sigma_{e,eff} = \sigma_{e} \frac{V_{e}}{\tau_{e}} \tag{32}$$

241 **2.4 Momentum and mass transport**

242 The Navier-Stokes (N-S) equation is implemented to simulate the gas flow and momentum
243 transport processes in the gas channels and porous electrodes/reforming layer [36]:

244 For gas channels, the N-S equation is presented as:

245 $$\rho \frac{\partial u}{\partial t} + \rho u \nabla u = -\nabla p + \nabla[\mu(\nabla u + (\nabla u)^T) - \frac{2}{3}\mu \nabla u] \tag{33}$$

For porous electrodes and the in-tube reforming layer, the N-S equation containing the Darcy's term is presented as:

$$\rho\frac{\partial u}{\partial t}+\rho u\nabla u=-\nabla p+\nabla[\mu(\nabla u+(\nabla u)^{T})-\frac{2}{3}\mu\nabla u]-\frac{\varepsilon\mu u}{k} \quad (34)$$

where k is permeability, m^2; ρ is gas density, $kg\cdot m^{-3}$; u is velocity vector, $m\cdot s^{-1}$; μ is dynamic viscosity, $kg\cdot m^{-1}\cdot s^{-1}$; ε is porosity. ρ and μ for the gas mixture can be further expressed as:

$$\rho=\sum_{i=1}^{N}y_i\rho_i \quad (35)$$

$$\mu=\sum_{j=1}^{N}y_i\mu_i \quad (36)$$

where ρ_i, μ_i and y_i are the density, dynamic viscosity, and molar friction of specie i, respectively.

The diffusion of species in channels (molecular diffusion) and porous electrodes/reforming layer (both molecular diffusion and Knudsen diffusion) are simulated by using the general Fick model [42]:

$$N_i=-\frac{1}{RT}\left(\frac{ky_iP}{\mu}\frac{\partial P}{\partial z}-D_{ij,eff}\frac{\partial(y_iP)}{\partial z}\right) \quad (37)$$

where k is permeability, m^2; y_i is the molar fraction of specie i; $D_{ij,eff}$ represents the effective binary diffusion coefficient, which can be further calculated as [43]:

$$D_{ij,eff}=\frac{\varepsilon}{\tau}(\frac{1}{D_{ij}}+\frac{1}{D_{ik}})^{-1} \quad (38)$$

$$D_{ij}=\frac{0.00143T^{1.75}}{2p\left(v_i^{1/3}+v_j^{1/3}\right)^2}\left(\frac{1}{M_i}+\frac{1}{M_j}\right)^{1/2} \quad (39)$$

$$D_{ik}=\frac{2}{3}r\sqrt{\frac{8RT}{\pi M_i}} \quad (40)$$

where D_{ij} is the binary diffusion coefficient, $m^2\cdot s^{-1}$; D_{ik} is the effective Knudsen diffusion coefficient, $m^2\cdot s^{-1}$; M_i is the molar mass of species i, $kg\cdot mol^{-1}$; r is the radius of electrode pores, m; v is special molecule diffusion volume of each species, m^3. The detailed material properties

can be found in Ref. [44-48].

2.5 Heat transfer

During operation, the cell performance and temperature distribution are significantly affected by the intense heat absorbing/releasing process due to the internal chemical/electrochemical reactions, the temperature distribution and heat transfer process in the cell is simulated by using the general heat balance equation [36]:

In channels:

$$\rho c_p u \cdot \nabla T + \nabla \cdot (-\lambda_g \nabla T) = 0 \tag{41}$$

In porous electrodes/reforming layer and electrolyte:

$$\rho c_p u \cdot \nabla T + \nabla \cdot (-\lambda_{eff} \nabla T) = Q \tag{42}$$

$$\lambda_{eff} = (1-\varepsilon)\lambda_s + \varepsilon \lambda_g \tag{43}$$

where c_p represents the specific heat capacity, $J \cdot mol^{-1} \cdot K^{-1}$; λ_g and λ_s represent the thermal conductivity ($W \cdot m^{-1} \cdot K^{-1}$) of gas species and solid phase, respectively. Q is the heat source term, representing the heat releasing/absorbing processes caused by chemical reactions and different overpotential losses. The heat source terms indicating the chemical reactions, electrochemical reactions, and ohmic loss can be calculated as [36]:

$$Q_{chem} = R_{chem} \cdot \Delta H_{chem} \tag{44}$$

$$Q_{elec} = (-T\Delta S) \cdot \frac{i}{nF} \tag{45}$$

$$Q_{ohmic} = -(i \cdot \nabla \varphi) \tag{46}$$

where R_{chem} represents the reaction rate of each chemical reaction; ΔH_{chem} indicates the enthalpy change in each chemical reaction; ΔS indicates the entropy change in each electrochemical reaction. The physical properties of each species and solid material can be found in Ref. [35,44,45,49].

289 **2.6 Boundary conditions and model validation**

290 The finite element method (COMSOL Multiphysics) is adopted to solve the 2D steady-
291 state model in this study, and Table 2 shows the boundary conditions used for the calculation.

292 Table 2 Boundary conditions in this study

Location	Boundary conditions
Anode/Anode channel interface	Ø=V_{cell}
Cathode/Cathode channel interface	Ø=0
Anode tube inlet	Specify the temperature, flow rate, and gas composition
Cathode channel inlet	Specify the temperature, flow rate, and gas composition
Anode channel outlet	Pressure outlet
Cathode channel outlet	Pressure outlet
Other surfaces	Insulated and adiabatic

293 In order to ensure the computational accuracy and reduce the solution time, grid-
294 independence check is performed and a grid with 470,000 degrees of freedom (Fig. 2(a)) is
295 adopted in the calculations. The electrochemical model of this study was validated through a
296 2D button SOEC model (Fig. 2(b)) [38]. While the chemical model was validated through a
297 2D fixed-bed reactor model (Fig. 2(c)) by using the parameters of glycerol conversion and H_2
298 selectivity [39]. The glycerol conversion and H_2 selectivity use for model validation are defined
299 as [39]:

300 $$Glycerol\ \ conversion, X_{Glycerol} = \frac{Carbon_{gas}}{3 \times Glycerol_{in}} \times 100\% \qquad (47)$$

301 $$H_2\ selectivity, S_{H_2} = \frac{moles\ of\ H_2\ in\ gas\ products}{moles\ of\ carbon\ in\ gas\ products} \times \frac{3}{7} \times 100\% \qquad (48)$$

302 The operating conditions used for model validation are listed in Table 3, and the parameters

in this study are given in Table 4. From Fig. 2(b) and Fig. 2(c), it is observed that the simulated results of the chemical and electrochemical models have good consistency with the experimental results, thus validating the model. This indicates that the assumptions and governing equations adopted in this study can reasonably describe the actual multiphysics processes in SOEC and can be used in calculations.

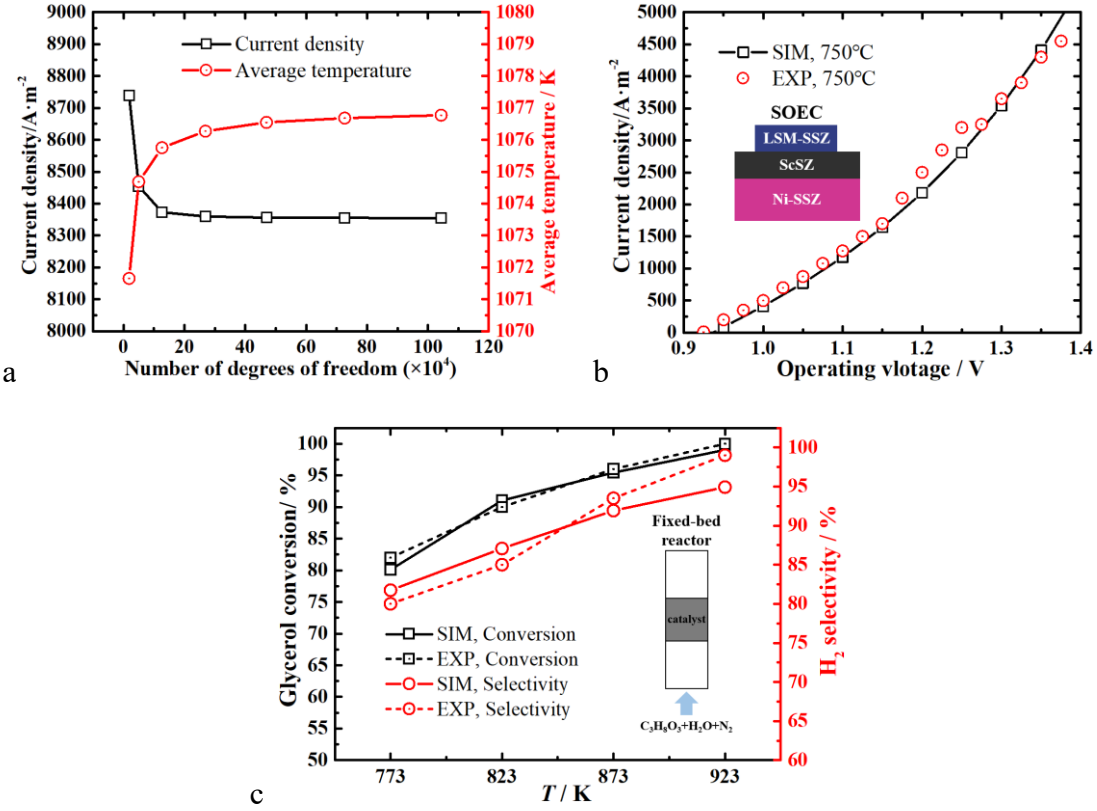

Fig.2 (a) Grid independence check; (b) model validation using button SOEC; (c) model validation using fixed-bed reactor

Table 3 Operating conditions in model validation

Parameters	Button SOEC model [38]	Fixed-bed reactor model [39]
Temperature	1023K	773~923K
Voltage	0.9~1.4 V	-
Inlet/Anode inlet	Air	$C_3H_8O_3$:H_2O:N_2=2%:18%:80%
Inlet/Anode flow rate	150 SCCM	95 SCCM

Cathode inlet	CO_2:H_2O:H_2:N_2 =28.6%:28.6%:14.3%:28.5%	-
Cathode flow rate	350 SCCM	-
Operating pressure	1 atm	1 atm

Table 4 Parameters in this study

Parameters	Value	Unit
Operating temperature	1023~1123	K
Anode inlet flow rate	50~150	SCCM
Cathode inlet flow rate	75~175	SCCM
Anode tube inlet	Unassisted system: Air Assisted system: 10%$C_3H_8O_3$+40%H_2O+50%N_2	-
Cathode inlet	H_2O/CO_2 (molar ratio 50%/50%)	-
Operating voltage	Unassisted system: 0.9~1.4 Assisted system: 0.45~0.65	V
Outlet pressure	1	atm

3 Results and discussions

3.1 Effects of operating voltage

Simulations of the glycerol-assisted co-electrolysis SOEC are carried out at different operating voltages, when the operating temperature is 1073 K, cathode flow rate is 150 SCCM, anode flow rate is 100 SCCM, anode glycerol molar fraction is 0.1 and cathode H_2O molar fraction is 0.5. From Fig. 3(a), when the operating voltage is changing from 0.45 V to 0.65 V, the current density is increasing from 3799 $A \cdot m^{-2}$ to 9524 $A \cdot m^{-2}$. This is significantly lower than that of the unassisted system (which needs to operate at 1.25 V and 1.43 V to achieve the same current density at 1073K, respectively, Fig. 3(b)), indicating that the use of glycerol to

assist the co-electrolysis process can save more than 55% of electrical energy, thus reducing the power consumption significantly. From Fig. 3(c), the larger operating voltage facilitates the electrochemical reactions in the cathode, increasing the conversion of H_2O and CO_2 from 14.7% and 3.8% at 0.45 V to 68.4% and 52.8% at 0.65 V, respectively. This leads to an increasing molar fraction of H_2 and CO at the cathode outlet to 0.33 and 0.27 (Fig. 3(c)), bring a higher yield of syngas. Besides, the higher current density also generates more heat, which raises the average temperature in the cell (Fig. 3(a)) and promotes the decomposition of glycerol in the in-tube reformer, bringing a higher in-tube glycerol conversion rate (Fig. 3(d)). From Fig. 3(d), when the operating voltage is increasing from 0.45 V to 0.65 V, the glycerol in the cell is completely converted (overall glycerol conversion ($X_{Glycerol}$) is 100%, reacting both at the in-tube reformer and the anode surface), and the increasing average temperature promotes a higher glycerol conversion in the in-tube reformer ($X_{Glycerol,in\text{-}tube}$ from 55.9% to 82.7%, reacting only at the in-tube reformer), which means that the in-tube reformer takes up the majority conversion of glycerol at higher operating voltages. Moreover, it can be seen from Fig. 3(e) and Fig. 3(f), the increasing glycerol conversion in the in-tube reformer at higher voltages (e.g. V_{cell}=0.65V) leads to a higher concentration of H_2 and CO at the entrance of the anode channel (also the anode corner), which provides more reactants for the electrolysis assisting reactions in the anode (Eqs. (7), (8)). While the larger current density at higher voltages (e.g. V_{cell}=0.65V) promotes the consumption of reactants (H_2 and CO) in the anode channel, making that at higher operating voltages, although the concentration of H_2 and CO at the entrance of the anode channel is higher, the larger current density promotes the rapid consumption of H_2 and CO in the anode channel, thus reducing the concentration of H_2 and CO at anode outlet, as shown in Fig. 3(d), Fig. 3(e) and Fig. 3(f). Fig. 3(g) shows the distribution of each anode species ($C_3H_8O_3$, H_2, H_2O, CO, and CO_2) along the anode main stream at different operating voltages. From Fig. 3(g), it can be seen that compared with the condition of V_{cell}=0.65V, the conversion of glycerol

in the anode tube is lower at V_{cell}=0.45V due to the lower average temperature, which leads to a lower H_2 and CO concentration at the entrance of anode channel (also the anode corner). And since there is still a part of glycerol not converted at the exit of inner tube, the remaining glycerol (44.1%) is further converted to H_2 and CO with H_2O at the anode electrolyte (Eqs. (5), (6)), leading to a further decrease of H_2O and an increase of H_2/CO concentrations after entering the anode channel as the operating voltage is 0.45V, as shown in Fig. 3(g). While when the operating voltage is 0.65V, as most of the glycerol has been converted in the in-tube reformer (82.7%), H_2 and CO are directly involved in the electrolysis assisting reactions (Eqs. (7), (8)) when the gas mixture enters the anode channel, leading to a rapid decrease of H_2/CO concentration and increase of H_2O/CO_2 concentration, as shown in Fig. 3(g). As the operating voltage increases, more heat is generated due to the larger current density, causing a higher cell temperature, as shown in Fig. 3(h). Fig. 3(i) shows the temperature distribution of the electrolyte along the anode main stream. It is worth noting that when the operating voltage is 0.6 V, the cell has a highly uniform internal temperature distribution (Fig. 3(i)), with the average temperature of 1073 K (Fig. 3(a)). This indicates that at this condition (V_{cell}=0.6V), the system not only reaches the overall internal thermal neutrality, but also has a highly uniform internal temperature distribution, eliminating significant temperature differences. The internal thermal neutrality means that the system does not require additional heating/cooling measures during operation; while the elimination of temperature differences facilitates the long-term operation of the system. This is important because large temperature differences may lead to electrolyte cracking or delamination between the electrolyte and electrodes during long-term operation, thus causing severe irreversible cell structural failure or even resulting in total breakdown to the system [50,51] (From Fig. 3(h), the main temperature difference is along the gas flow, rather than vertical to the gas flow). This indicates that it has great potential to eliminate the temperature difference and improve the energy conversion efficiency through the proper design

of the geometrical and operational parameters of the in-tube reformer, which is essential for the long-term operation of the system. Further studies on the in-tube reformer will be conducted in the future so as to obtain the optimal system performance and significantly eliminate the temperature difference, even achieving the complete homogeneous temperature operation within the cell.

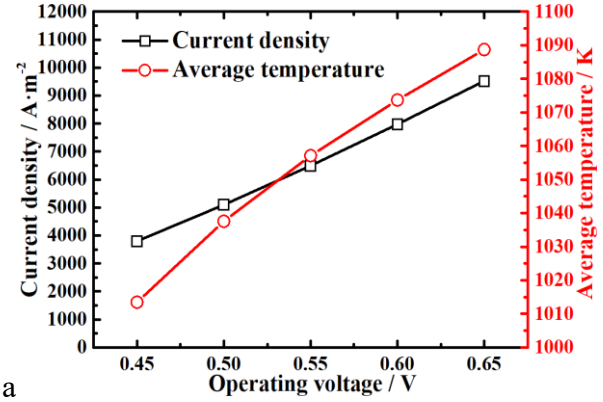

a

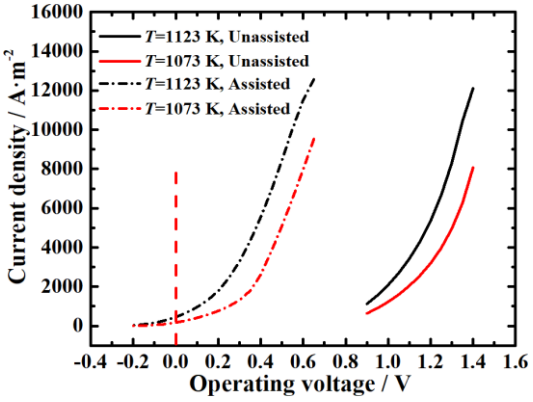

b

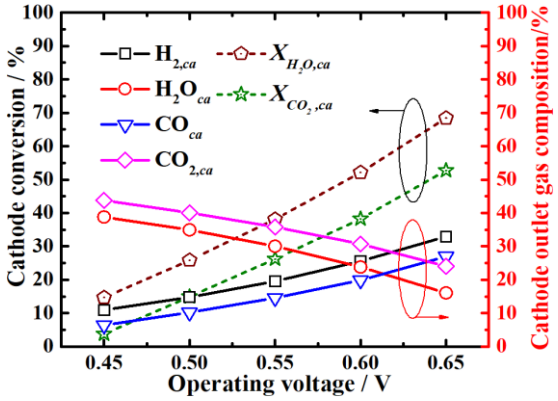

c

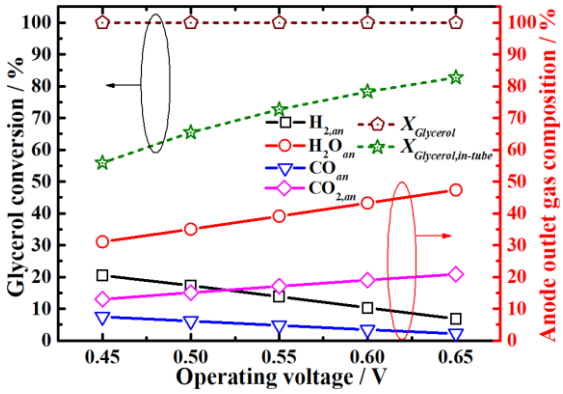

d

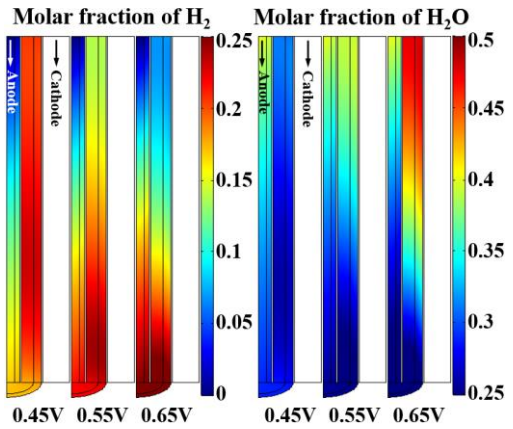

e

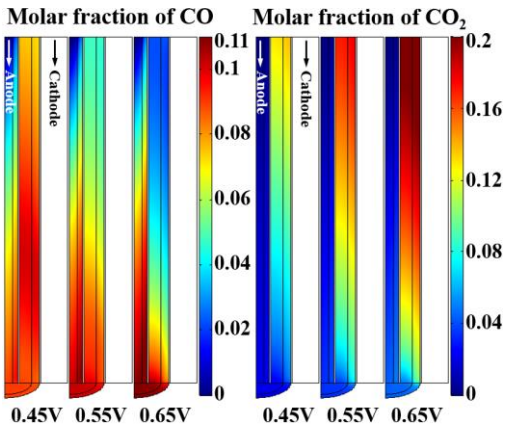

f

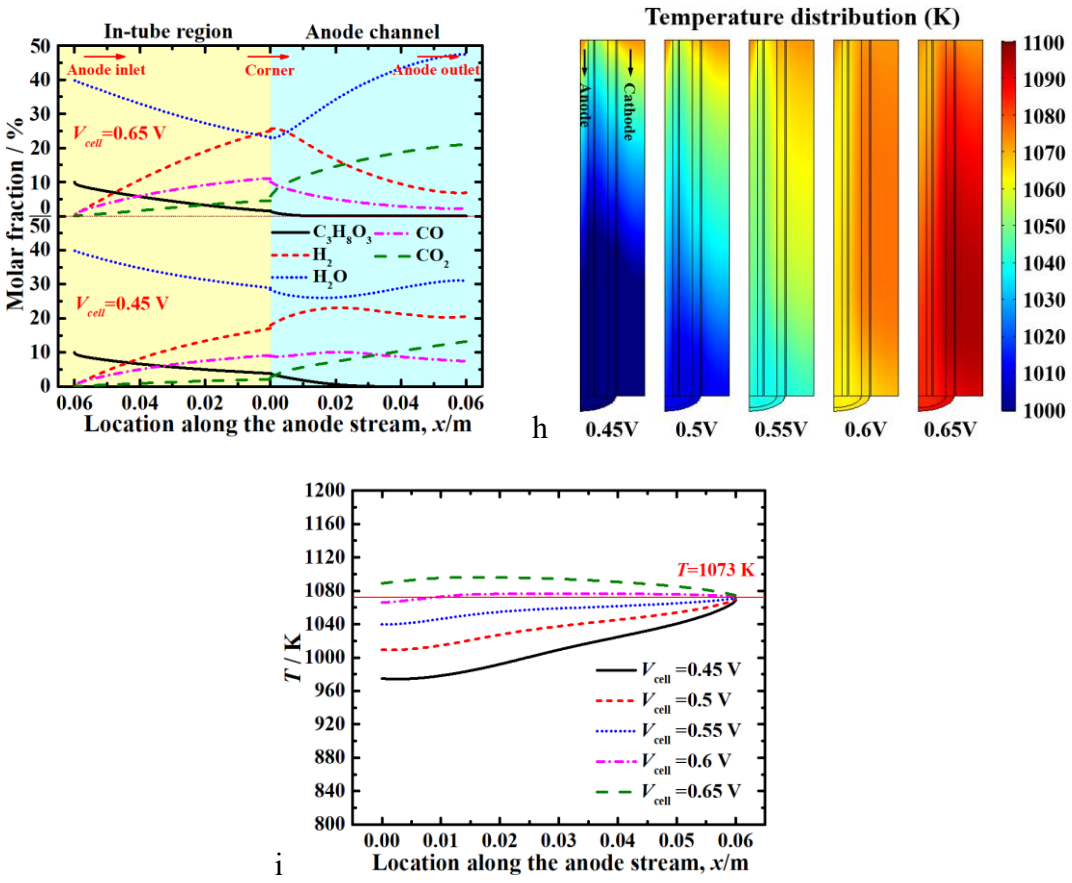

g h i

Fig.3 Effects of operating voltage on: (a) current density and average temperature; (b) I-V curve of assisted system and unassisted system; (c) cathode conversion and cathode outlet gas composition; (d) glycerol conversion and anode outlet gas composition; (e) anode H_2 and H_2O distribution; (f) anode CO and CO_2 distribution; (g) molar fraction of each species along the anode main stream; (h) temperature distribution; (i) temperature distribution in the electrolyte

3.2 Effects of operating temperature (gas inlet temperature)

The chemical/electrochemical reaction kinetics are significantly affected by the operating temperature. Simulations are carried out at different operating temperatures when the operating voltage is 0.6 V, cathode flow rate is 150 SCCM, anode flow rate is 100 SCCM, anode glycerol molar fraction is 0.1 and cathode H_2O molar fraction is 0.5. From Fig. 4(a), it is clear that as the operating temperature increases from 1023 K to 1123 K, the kinetics of electrochemical reactions are promoted, increasing the current density from 4155 $A \cdot m^{-2}$ to 11529 $A \cdot m^{-2}$. This

promotes the co-electrolysis process of H_2O and CO_2 at the cathode TPBs, increasing the conversion of H_2O and CO_2 (as shown in Fig. 4(b)) from 24.1% and 14.0% to 83.5% and 70.9%, respectively, leading to a further increase of the H_2 and CO molar fraction at the cathode outlet to 0.40 and 0.38 as the operating temperature increases from 1023 K to 1123 K. Meanwhile, from Fig. 4(c), the increasing operating temperature also facilitates the glycerol conversion in the in-tube reformer, increasing the in-tube glycerol conversion from 62.4% to 84.9% when the temperature increases from 1023 K to 1123 K. From Fig. 4(d) and Fig. 4(e), it is clear that as temperature increases, the larger in-tube glycerol conversion increases the H_2 and CO concentrations at the anode channel entrance (also the anode corner); while the higher current density leads to a rapid consumption of anode H_2 and CO concentrations at this time. As shown in Fig. 4(f), the glycerol is not fully decomposed in the inner tube at lower operating temperature (e.g. T=1023K), resulting in a higher glycerol concentration at the exit of the inner tube (also the anode corner). After entering the anode channel, the remaining glycerol continues to react with H_2O and is fully decomposed at the position of x=0.01 m (Fig. 4(f)), making the highest H_2 concentration and the lowest H_2O concentration in this region. Subsequently, H_2 and CO in the anode channel are gradually consumed due to the electrochemical reaction, however, the lower current density at T=1023 K leads to a higher H_2 and CO concentration at the anode outlet, as shown in Fig. 4(f). Fig. 4(g) and Fig. 4(h) show the temperature distribution of the assisted and unassisted systems, both of which are operated at the same operating temperature and same current density (4155 $A \cdot m^{-2}$ at 1023K, 7979 $A \cdot m^{-2}$ at 1073K, and 11529 $A \cdot m^{-2}$ at 1123K). From Fig. 4(g) and Fig. 4(h), it is clear that compared to the unassisted system, the glycerol assisted system with the in-tube reformer not only reaches the same current density at lower operating voltages as the unassisted system (Fig. 3(b)), but also has a more uniform temperature distribution (except for the remarkable temperature difference of the assisted system due to excessive heat absorption at T=1123K), significantly reducing the temperature

difference inside the cell, which demonstrates the prospect for the long-term efficient electrolysis process by using this assisted method.

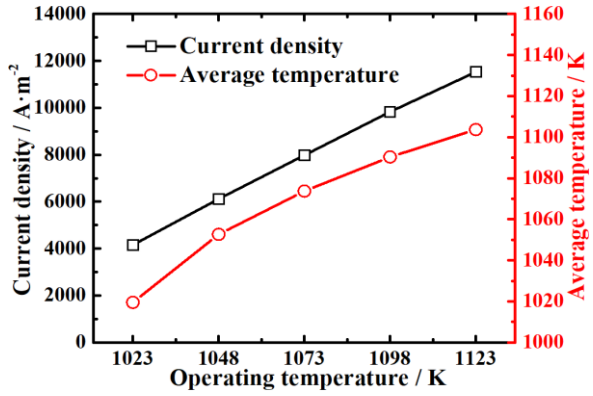

a

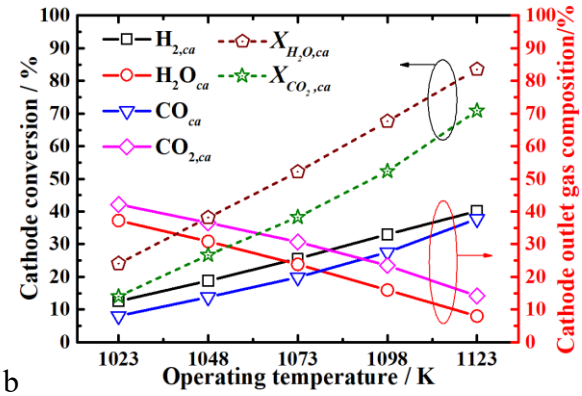

b

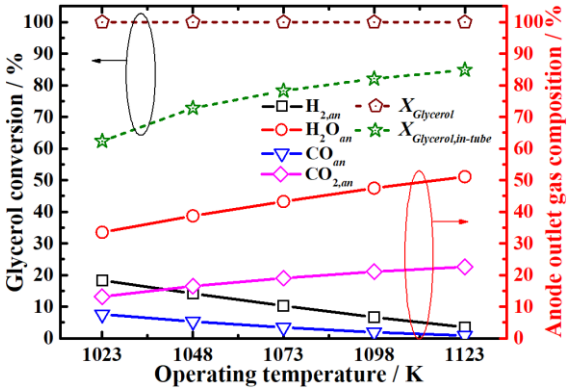

c

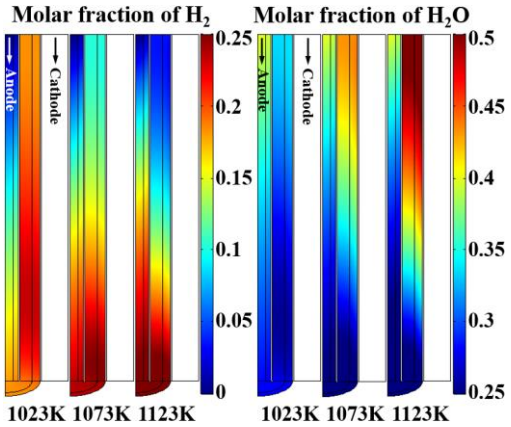

d

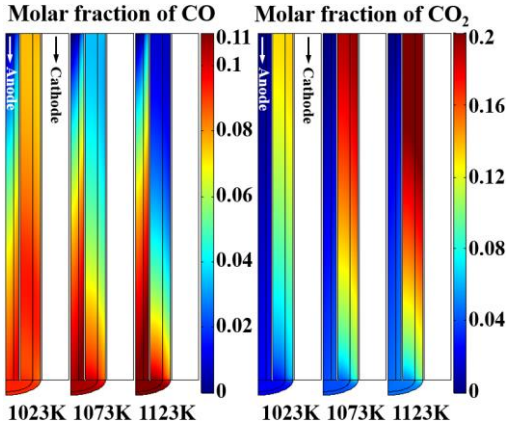

e

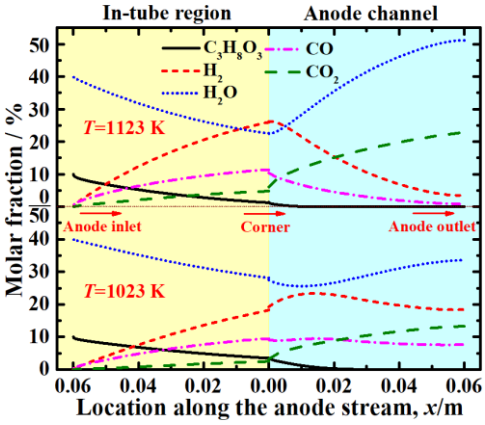

f

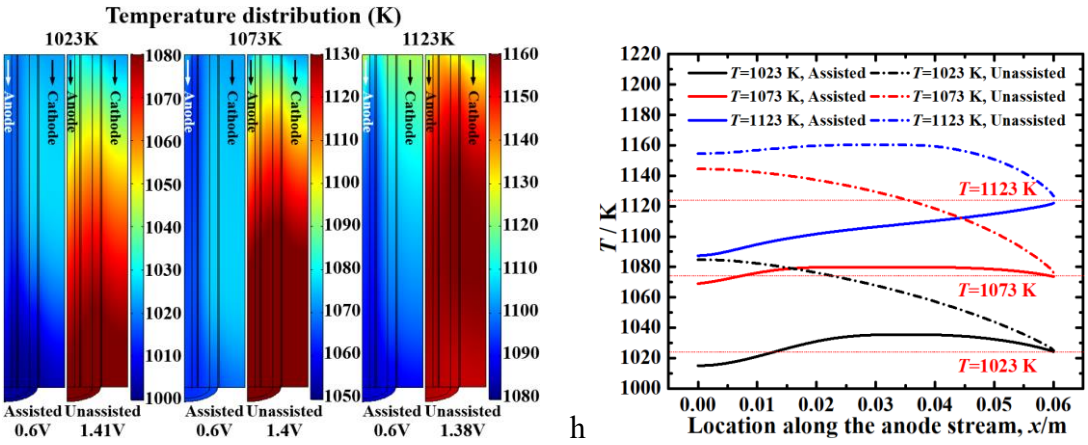

426 g h

427 Fig.4 Effects of operating temperature on: (a) current density and average temperature; (b)
428 cathode conversion and cathode outlet gas composition; (c) glycerol conversion and anode
429 outlet gas composition; (d) anode H_2 and H_2O distribution; (e) anode CO and CO_2
430 distribution; (f) molar fraction of each species along the anode main stream; (g) temperature
431 distribution of the assisted and unassisted systems; (h) temperature distribution in the
432 electrolyte

433 **3.3 Effects of anode flow rate**

434 During operation, a gas mixture of $C_3H_8O_3/H_2O/N_2$ is supplied to the anode as the assisted
435 fuel, with a molar ratio of 10%:40%:50%. Simulations are carried out at different anode flow
436 rates when the operating voltage is 0.6 V, cathode flow rate is 150 SCCM, operating
437 temperature is 1073 K, anode glycerol molar fraction is 0.1 and cathode H_2O molar fraction is
438 0.5. From Fig. 5(a), it is clear that as anode flow rate increases from 50 SCCM to 100 SCCM,
439 more glycerol is provided and decomposed so as to provide more auxiliary fuels (H_2 and CO)
440 to the anode, which promotes the anode electrochemical reactions (Eqs. (7), (8)) and leads to a
441 higher current density. While as the anode flow rate is further increasing from 100 SCCM to
442 150 SCCM, the further improvement of the electrochemical reactions has not been observed.
443 Instead, due to the highly heat-absorbing glycerol reforming reaction (Eq. (4)), the sufficient
444 or even excessive glycerol is reformed thus lowering the average temperature in the cell, which

decreases the current density in Fig. 5(a). Meanwhile, from Fig. 5(b), the conversion of H_2O and CO_2 in the cathode shows the same trend with the current density, reaching the maximum of 52.1% and 38.3% at Q_{an}=100 SCCM, respectively. Besides, from Fig. 5(c), the anode velocity and absolute glycerol content increase as the anode flow rate is changing from 50 SCCM to 150 SCCM, leading to a lower glycerol conversion in the inner tube. And as more glycerol is converted at the anode electrode after leaving the in-tube reformer, it makes the peak of H_2 and CO concentrations gradually move downstream in the anode channel, resulting in a higher H_2 and CO concentrations at the anode outlet, as shown in Fig. 5(d), Fig. 5(e) and Fig. 5(f). From Fig. 5(g) and Fig. 5(h), it is clear that at lower anode flow rates (e.g. Q_{an}=50 SCCM or Q_{an}=100 SCCM), the anode has sufficient auxiliary fuels (H_2 and CO) due to the large conversion of glycerol in the in-tube reformer ($X_{an,GL}$>78%, Fig. 5(c)), which promotes the anode electrochemical reactions and increases the temperature in the anode. However, at higher anode flow rates (e.g. Q_{an}=150 SCCM), more glycerol is reformed at the anode electrode and higher gas flow rate also carries away more heat, resulting in a lower temperature at the anode electrode (especially at x<0.03 m), which affects the anode electrochemical reaction kinetics and causes a significant temperature unevenness, as shown in Fig. 5(g) and Fig. 5(h). Therefore, the optimal anode flow rate is Q_{an}=70~110 SCCM, at which the cell has good electrochemical performance and good temperature uniformity simultaneously.

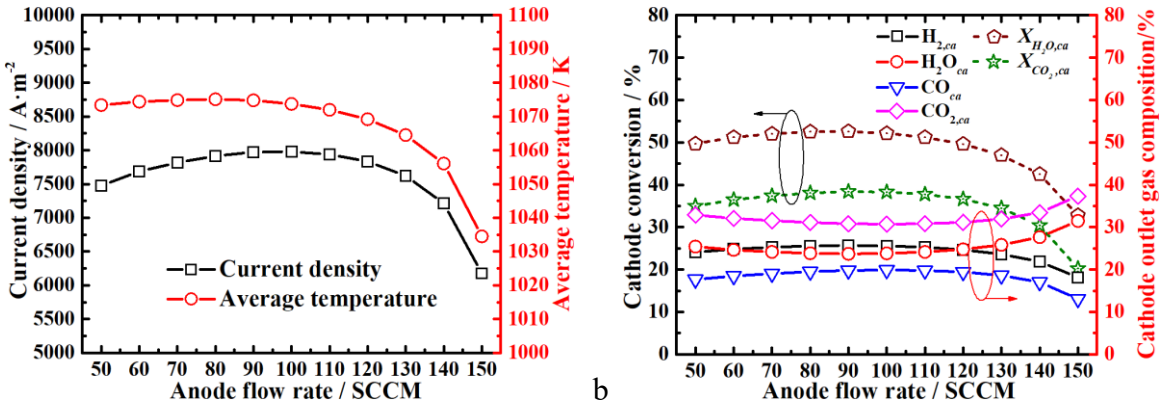

a b

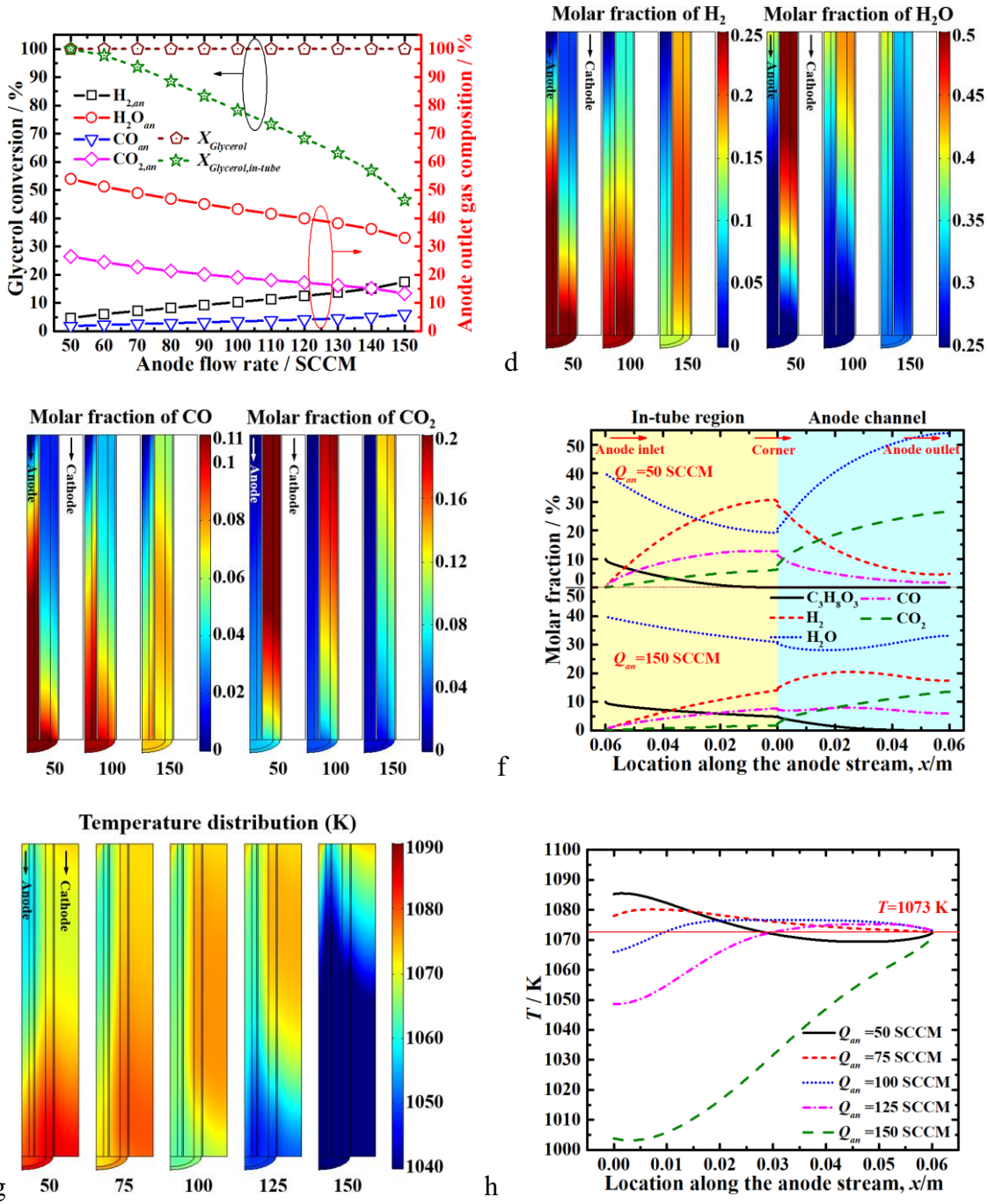

Fig.5 Effects of anode flow rate on: (a) current density and average temperature; (b) cathode conversion and cathode outlet gas composition; (c) glycerol conversion and anode outlet gas composition; (d) anode H_2 and H_2O distribution; (e) anode CO and CO_2 distribution; (f) molar fraction of each species along the anode main stream; (g) temperature distribution; (h) temperature distribution in the electrolyte

3.4 Effects of cathode flow rate

A mixture of H_2O and CO_2 is supplied to the cathode as reactants for the co-electrolysis process. Simulations are carried out at different cathode flow rates when the operating voltage is 0.6 V, operating temperature is 1073 K, anode flow rate is 100 SCCM, anode glycerol molar fraction is 0.1 and cathode H_2O molar fraction is 0.5. Increasing the cathode flow rate from 75 SCCM to 175 SCCM promotes the electrolysis reactions (Eqs. (1), (2)) to the forward direction because more reactants are supplied into the cathode, which increases the current density from 6552 $A \cdot m^{-2}$ to 7929 $A \cdot m^{-2}$, thus higher heat generation rate and higher cell average temperature (Fig. 6(a)). Besides, from Fig. 6(b), the insufficient reactants for the electrolysis reaction leads to high cathode H_2O and CO_2 conversions at lower cathode flow rates (e.g. Q_{ca}=75 SCCM), while the conversion of H_2O and CO_2 decreases with increasing cathode flow rate as sufficient reactant is passed into the cathode. As for the anode, increasing the cathode flow rate increases the glycerol conversion in the in-tube reformer gradually from 63.1% to 76.7% due to the increasing average temperature. From Fig. 6(c), the higher current density at large cathode flow rate (e.g. Q_{ca}=125 SCCM) leads to a faster consumption of H_2 and CO in the anode channel, resulting in a lower H_2/CO content in the anode outlet. However, when the cathode flow rate exceeds 125 SCCM, no significant change in glycerol conversion and anode outlet gas composition is observed (Fig. 6(c), Fig. 6 (d) and Fig. 6 (e)), as further increasing the cathode flow rate does not lead to an obvious increase in the average temperature and current density (Fig. 6(a)). From Fig. 6(f), at lower cathode flow rates (e.g. Q_{ca}=75 SCCM), the lack of reactants for the cathode electrochemical reactions leads to a lower electrochemical reaction intensity and cell temperature (especially downstream of the cathode, Fig. 6(g)). Therefore, the remaining glycerol continues to be converted after entering the anode channel, resulting in a delayed peak of H_2 concentration (x=0.01 m), while the lower current density reduces the consumption of H_2 and CO, resulting in a higher H_2 and CO concentration at the anode outlet compared to the condition of Q_{ca}=175 SCCM (Fig. 6(f)). And since the glycerol reforming

reaction is heat-absorbing, the conversion of glycerol at the anode electrode at lower flow rates (e.g. Q_{ca}=75 SCCM) further reduces the temperature at the cathode downstream region, resulting in a significant temperature difference in the cell, as shown in Fig. 6(g) and Fig. 6(h). Therefore, the lower cathode flow rate should be prevented to avoid negative effects on the electrochemical performance and temperature distribution of the cell, and the optimal cathode flow rate is Q_{ca}=125~175 SCCM.

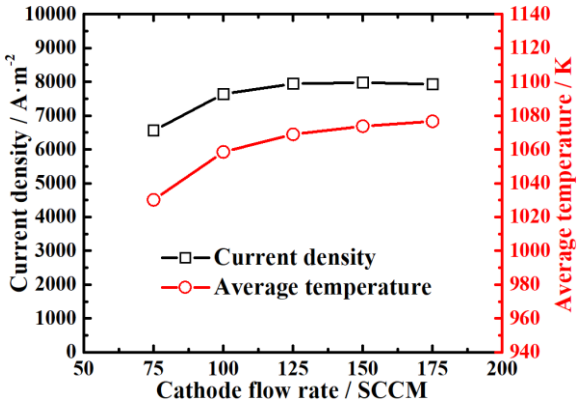

a

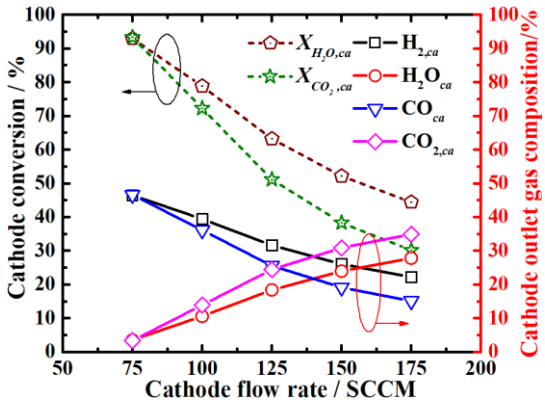

b

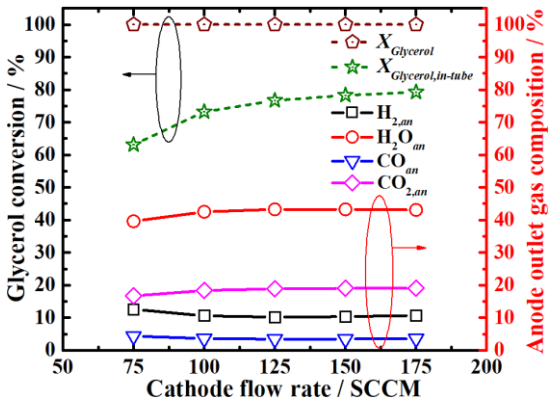

c

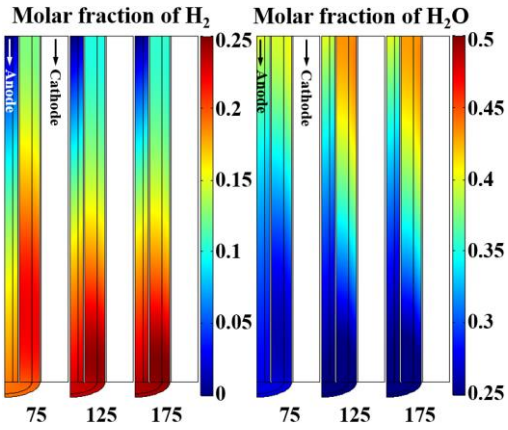

d

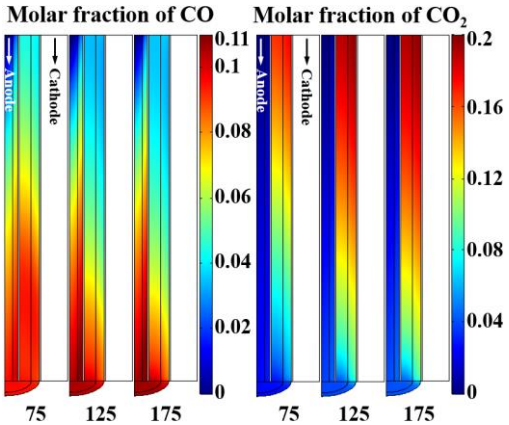

e

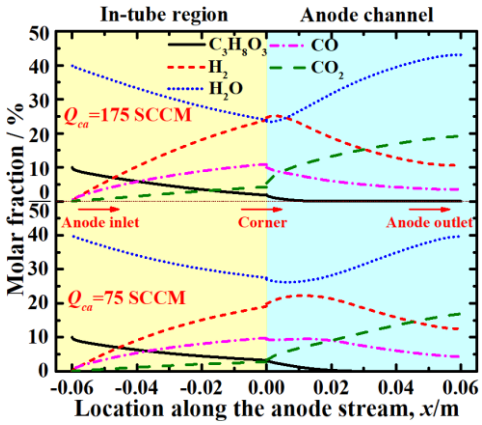

f

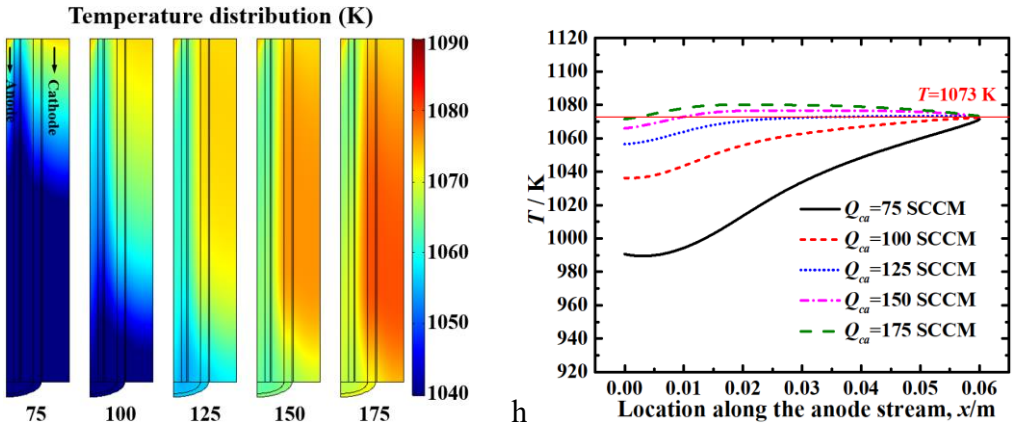

Fig.6 Effects of cathode flow rate on: (a) current density and average temperature; (b) cathode conversion and cathode outlet gas composition; (c) glycerol conversion and anode outlet gas composition; (d) anode H_2 and H_2O distribution; (e) anode CO and CO_2 distribution; (f) molar fraction of each species along the anode main stream; (g) temperature distribution; (h) temperature distribution in the electrolyte

3.5 Effects of anode glycerol molar fraction

Since the auxiliary fuels (H_2 and CO) in the anode are produced by the reforming reaction of glycerol and H_2O, the molar fraction of glycerol in the anode directly affects the supply of auxiliary fuels. Simulations are carried out at different anode glycerol molar fractions when the operating voltage is 0.6 V, operating temperature is 1073 K, cathode flow rate is 150 SCCM, anode flow rate is 100 SCCM and cathode H_2O molar fraction is 0.5. From Fig. 7(a), as the glycerol molar fraction is increasing from 0.05 to 0.15, more auxiliary fuels (H_2 and CO) are generated due to more glycerol being converted, which brings a larger current density. While when the molar fraction of glycerol is further increasing from 0.15 to 0.25, more heat is consumed due to the decomposition of glycerol, which makes the average temperature decrease rapidly and also affects the intensity of the electrochemical reactions, causing a decrease in the current density (Fig. 7(a)). And the cathode H_2O/CO_2 conversion shows the same trend with the current density, as shown in Fig. 7(b). As for the anode, the increasing glycerol molar fraction decreases the glycerol conversion, even leading to the incomplete decomposition of

glycerol in the anode (Fig. 7(c)). From Fig. 7(c), Fig. 7(d), Fig. 7(e) and Fig. 7(f), it is clear that due to the continuous conversion of sufficient or even excessive glycerol in the anode channel, the concentration of H_2 and CO in the anode channel increases continuously with the increasing glycerol molar fraction, resulting in a high concentration of H_2 and CO at the anode outlet. Besides, from Fig. 7(g) and Fig. 7(h), due to the highly heat absorption of the glycerol reforming reaction (Eq. (4)), the temperature in the cell gradually decreases (especially at x<0.03 m) as glycerol molar fraction is changing from 0.15 to 0.25, resulting in a significant temperature unevenness. Therefore, the optimal anode glycerol molar fraction is $X_{an,GL}$=0.05~0.15.

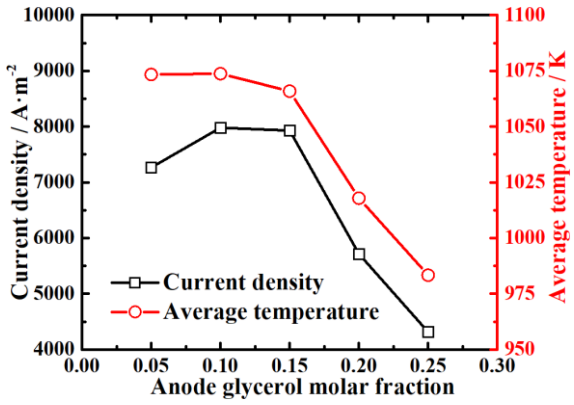

a

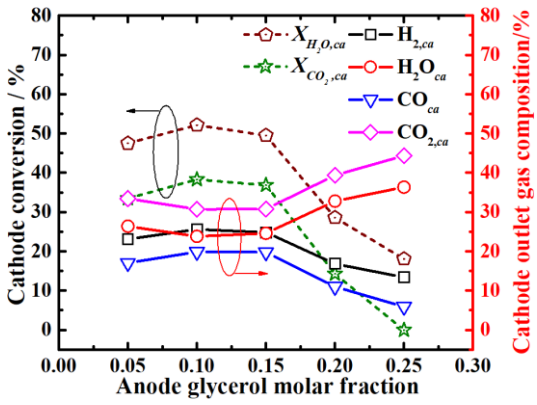

b

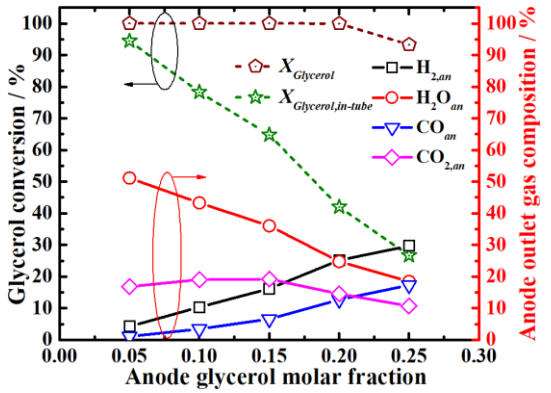

c

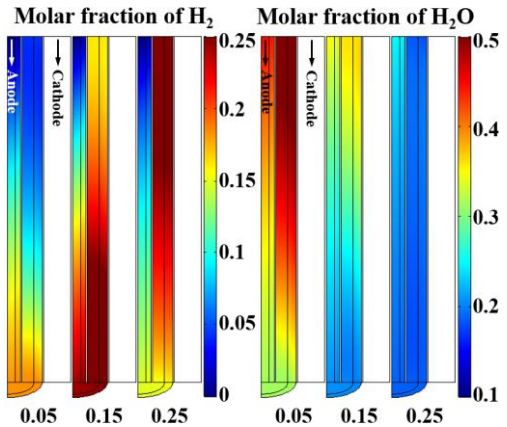

d

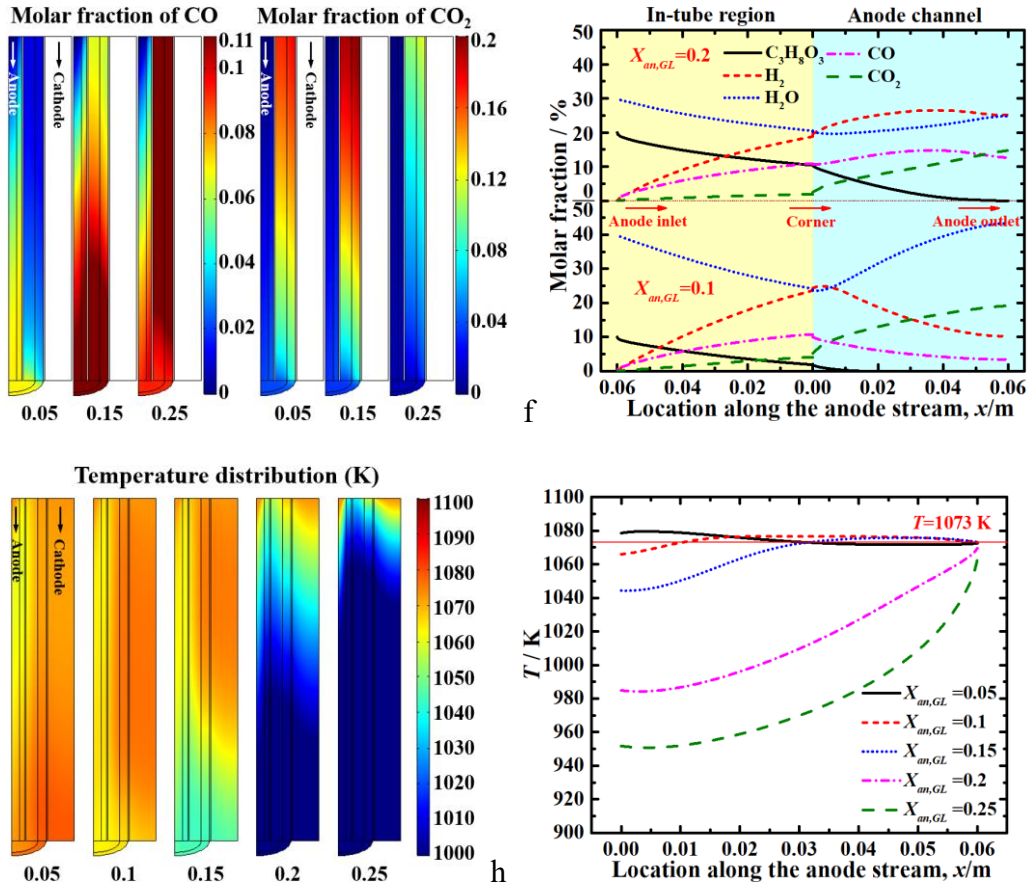

Fig.7 Effects of anode glycerol molar fraction on: (a) current density and average temperature; (b) cathode conversion and cathode outlet gas composition; (c) glycerol conversion and anode outlet gas composition; (d) anode H_2 and H_2O distribution; (e) anode CO and CO_2 distribution; (f) molar fraction of each species along the anode main stream; (g) temperature distribution; (h) temperature distribution in the electrolyte

3.6 Effects of cathode H_2O molar fraction

During operation, the ratio of H_2O and CO_2 at the cathode inlet can be changed as needed, so as to adjust the ratio of H_2 and CO in the syngas at the cathode outlet. Simulations are carried out at different cathode H_2O molar fractions when the operating voltage is 0.6 V, operating temperature is 1073 K, cathode flow rate is 150 SCCM, anode flow rate is 100 SCCM and anode glycerol molar fraction is 0.1. From Fig. 8(a), the current density and average temperature increases with increasing cathode H_2O molar fraction because the electrolysis of

H_2O has better electrochemical kinetics in the co-electrolysis of H_2O and CO_2 [52]. And the higher current density promotes the electrolysis of H_2O and CO_2 at the cathode TPBs, leading to a higher cathode conversion of H_2O and CO_2, as shown in Fig. 8(b). Besides, the higher current density and average temperature not only promote the conversion of glycerol in the in-tube reformer, but also accelerate the consumption of H_2 and CO in anode, leading to the decrease of H_2 and CO concentration at anode outlet, as shown in Fig. 8(c), Fig. 8(d), Fig. 8(e) and Fig. 8(f). Moreover, the increasing cathode H_2O content increases the internal cell temperature (Fig. 8(g), especially in the middle region of the cell, due to the counter-flow arrangement of the anode cathode channels). From Fig. 8(h), it is clear that both too small and too large H_2O contents in the cathode will cause significant temperature non-uniform distribution, so the ratio of cathode H_2O needs to be controlled properly, and the optimal cathode H_2O molar fraction is $X_{ca,H2O}$=0.4~0.6.

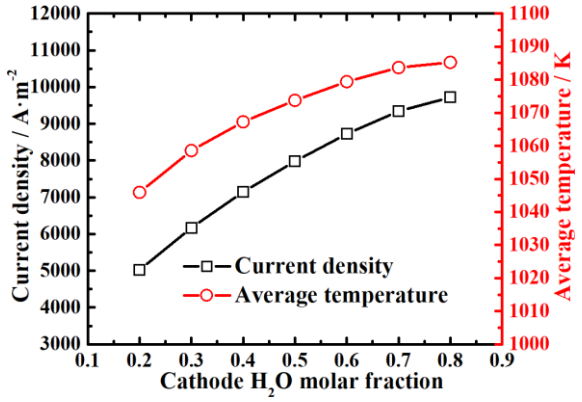

a

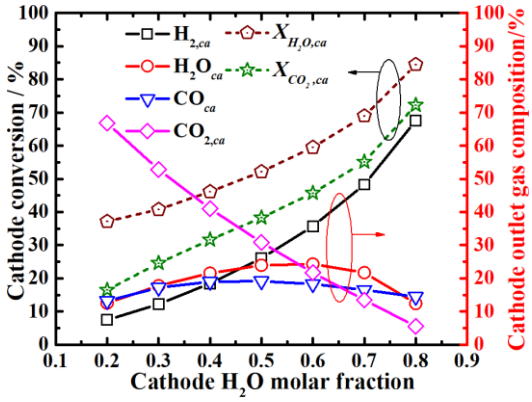

b

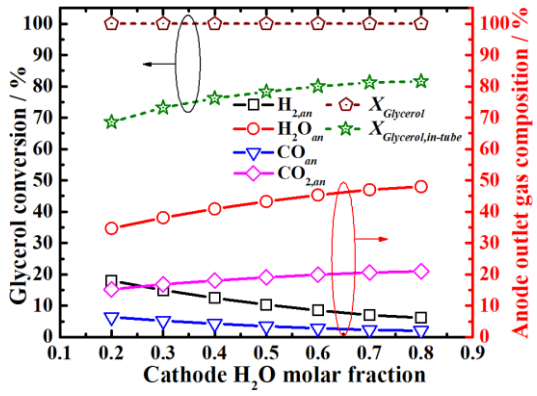

c

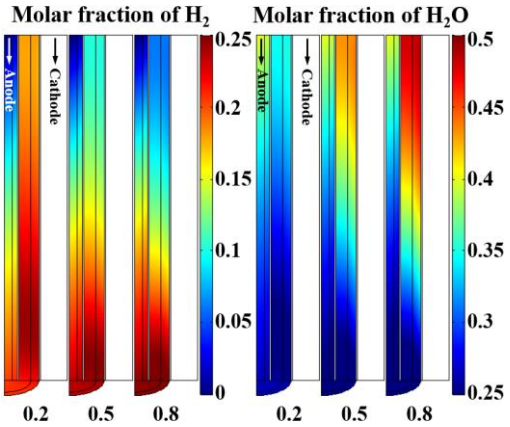

d

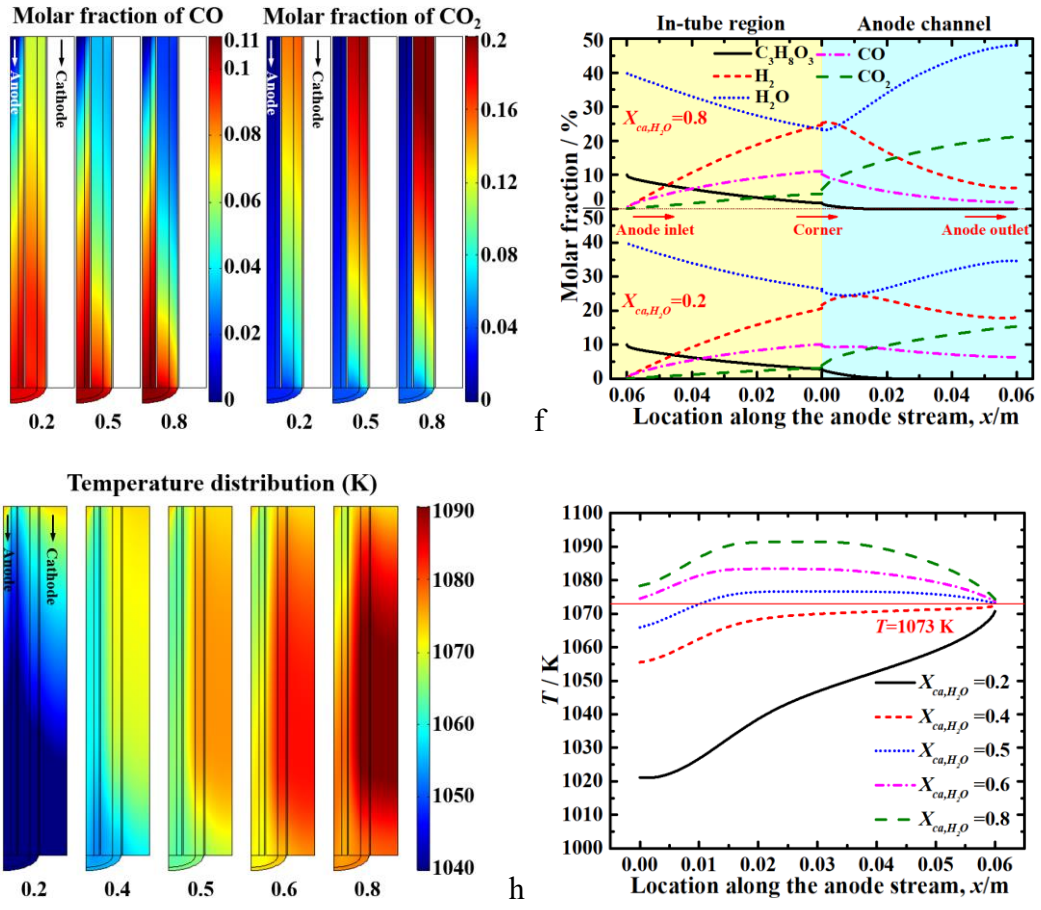

Fig.8 Effects of cathode H_2O molar fraction on: (a) current density and average temperature; (b) cathode conversion and cathode outlet gas composition; (c) glycerol conversion and anode outlet gas composition; (d) anode H_2 and H_2O distribution; (e) anode CO and CO_2 distribution; (f) molar fraction of each species along the anode main stream; (g) temperature distribution; (h) temperature distribution in the electrolyte

4 Conclusions

A 2D multi-physics model was developed to study the glycerol-assisted SOEC co-electrolysis process, with a novel in-tube reformer to improve the fuel utilization and reduce the temperature difference in the cell. The model fully considers the flow, diffusion, chemical and electrochemical processes and thermal effects in the SOEC. The effects of operating voltage, operating temperature, anode/cathode inlet flow rate and gas composition on the electrochemical performance and temperature distribution of the system were studied and

analyzed.

It is found that the operating voltage of the unassisted SOEC system can be significantly reduced (from 1.43 V to 0.65 V at 9524 $A \cdot m^{-2}$ and 1073K) by using the glycerol-assisted co-electrolysis process, thus saving over 55% of electrical energy. Besides, the increasing operating voltage, operating temperature and cathode H_2O molar fraction will promote the co-electrolysis process in the system, leading to a higher cathode H_2O/CO_2 conversion; while the anode/cathode flow rate and anode glycerol molar fraction all have the optimal values (Q_{an}=70~110 SCCM, Q_{ca}=125~175 SCCM and $X_{an,GL}$=0.05~0.15), with good electrochemical performance and uniform temperature distribution simultaneously. Finally, the in-tube reformer can significantly reduce the temperature difference inside the cell, and by precisely controlling the structural and operational parameters of the system, a more uniform internal temperature distribution can be obtained, even allowing the system to be operated at homogeneous temperature conditions.

Overall, this study provides an insight of the glycerol-assisted SOEC co-electrolysis system. And a novel in-tube reformer with high efficiency, compact size, easy fabrication, and high flexibility is proposed to improve electrochemical reactions and reduce internal temperature difference in SOEC. The system can effectively reduce the electrical energy consumption and enhance the performance and long-term stability during SOEC co-electrolysis, which can facilitate efficient glycerol utilization and CO_2 recovery, as well as producing green syngas by using renewable electricity.

601 **Acknowledgements**

602 M. NI thanks the grants (Project Number: N_PolyU552/20) from Research Grants Council,
603 University Grants Committee, Hong Kong SAR.

604

605

606 **Reference**

607 [1] Shahsavari A, Akbari M. Potential of solar energy in developing countries for reducing
608 energy-related emissions[J]. Renewable and Sustainable Energy Reviews, 2018, 90: 275-
609 291. https://doi.org/10.1016/j.rser.2018.03.065.

610 [2] Yang XJ, Hu H, Tan T, et al. China's renewable energy goals by 2050[J]. Environmental
611 Development, 2016, 20: 83-90. https://doi.org/10.1016/j.envdev.2016.10.001.

612 [3] Gross R, Leach M, Bauen A. Progress in renewable energy[J]. Environment international,
613 2003, 29(1): 105-122. https://doi.org/10.1016/S0160-4120(02)00130-7.

614 [4] Barton JP, Infield DG. Energy storage and its use with intermittent renewable energy[J].
615 IEEE transactions on energy conversion, 2004, 19(2): 441-448.
616 https://doi.org/10.1109/TEC.2003.822305.

617 [5] Amrouche SO, Rekioua D, Rekioua T, et al. Overview of energy storage in renewable
618 energy systems[J]. International journal of hydrogen energy, 2016, 41(45): 20914-20927.
619 https://doi.org/10.1016/j.ijhydene.2016.06.243.

620 [6] Olabi AG. Renewable energy and energy storage systems[J]. Energy, 2017, 136: 1-6.
621 https://doi.org/10.1016/j.energy.2017.07.054.

622 [7] Buttler A, Spliethoff H. Current status of water electrolysis for energy storage, grid
623 balancing and sector coupling via power-to-gas and power-to-liquids: A review[J].
624 Renewable and Sustainable Energy Reviews, 2018, 82: 2440-2454.
625 https://doi.org/10.1016/j.rser.2017.09.003.

626 [8] Li YH, Li YP, Zhang SW, et al. Mutual Conversion of CO–CO2 on a Perovskite Fuel
627 Electrode with Endogenous Alloy Nanoparticles for Reversible Solid Oxide Cells[J]. ACS
628 Applied Materials & Interfaces, 2022, 14(7): 9138-9150.
629 https://doi.org/10.1021/acsami.1c23548.

630 [9] Ormerod RM. Solid oxide fuel cells[J]. Chemical Society Reviews, 2003, 32(1): 17-28.

https://doi.org/10.1039/B105764M.

[10] Ni M, Leung MKH, Leung DYC. Technological development of hydrogen production by solid oxide electrolyzer cell (SOEC)[J]. International journal of hydrogen energy, 2008, 33(9): 2337-2354. https://doi.org/10.1016/j.ijhydene.2008.02.048.

[11] Fu Q, Mabilat C, Zahid M, et al. Syngas production via high-temperature steam/CO2 co-electrolysis: an economic assessment[J]. Energy & Environmental Science, 2010, 3(10): 1382-1397. https://doi.org/10.1039/C0EE00092B.

[12] Hauch A, Küngas R, Blennow P, et al. Recent advances in solid oxide cell technology for electrolysis[J]. Science, 2020, 370(6513): eaba6118. https://doi.org/10.1126/science.aba6118.

[13] Yu M, Budiyanto E, Tüysüz H. Principles of water electrolysis and recent progress in cobalt‐, nickel‐, and iron‐based oxides for the oxygen evolution reaction[J]. Angewandte Chemie International Edition, 2022, 61(1): e202103824. https://doi.org/10.1002/anie.202103824.

[14] Zheng Y, Zhao CH, Wu T, et al. Enhanced oxygen reduction kinetics by a porous heterostructured cathode for intermediate temperature solid oxide fuel cells[J]. Energy and AI, 2020, 2: 100027. https://doi.org/10.1016/j.egyai.2020.100027.

[15] Martinez-Frias J, Pham AQ, Aceves SM. A natural gas-assisted steam electrolyzer for high-efficiency production of hydrogen[J]. International Journal of Hydrogen Energy, 2003, 28(5): 483-490. https://doi.org/10.1016/S0360-3199(02)00135-0.

[16] Yang C, Li J, Newkirk J, et al. Co-electrolysis of H 2 O and CO 2 in a solid oxide electrolysis cell with hierarchically structured porous electrodes[J]. Journal of Materials Chemistry A, 2015, 3(31): 15913-15919. https://doi.org/10.1039/C5TA03264D.

[17] Wang M, Wang Z, Gong X, et al. The intensification technologies to water electrolysis for hydrogen production–A review[J]. Renewable and sustainable energy reviews, 2014, 29:

573-588. https://doi.org/10.1016/j.rser.2013.08.090.

[18] Lei L, Wang Y, Fang S, et al. Efficient syngas generation for electricity storage through carbon gasification assisted solid oxide co-electrolysis[J]. Applied Energy, 2016, 173: 52-58. https://doi.org/10.1016/j.apenergy.2016.03.116.

[19] Xu HR, Chen B, Ni M. Modeling of direct carbon-assisted solid oxide electrolysis cell (SOEC) for syngas production at two different electrodes[J]. Journal of The Electrochemical Society, 2016, 163(11): F3029. https://doi.org/10.1149/2.0041611jes.

[20] Wang W, Vohs JM, Gorte RJ. Hydrogen production via CH4 and CO assisted steam electrolysis[J]. Topics in Catalysis, 2007, 46: 380-385. https://doi.org/10.1007/s11244-007-9005-8.

[21] Wang W, Gorte RJ, Vohs JM. Analysis of the performance of the electrodes in a natural gas assisted steam electrolysis cell[J]. Chemical engineering science, 2008, 63(3): 765-769. https://doi.org/10.1016/j.ces.2007.10.026.

[22] Wang Y, Liu T, Lei L, et al. Methane assisted solid oxide co-electrolysis process for syngas production[J]. Journal of Power Sources, 2017, 344: 119-127. https://doi.org/10.1016/j.jpowsour.2017.01.096.

[23] Liu F, Wang T, Li J, et al. Elevated-temperature bio-ethanol-assisted water electrolysis for efficient hydrogen production[J]. Chemical Engineering Journal, 2022, 434: 134699. https://doi.org/10.1016/j.cej.2022.134699.

[24] Pagliaro M, Ciriminna R, Kimura H, et al. From glycerol to value‐added products[J]. Angewandte Chemie International Edition, 2007, 46(24): 4434-4440. https://doi.org/10.1002/anie.200604694.

[25] Tan HW, Aziz ARA, Aroua MK. Glycerol production and its applications as a raw material: A review[J]. Renewable and sustainable energy reviews, 2013, 27: 118-127. https://doi.org/10.1016/j.rser.2013.06.035.

[26] Bhatia L. Glycerol and its derivatives (propanediol, glycerolcarbonate, epichlorohydrin): implicit role in bioeconomy[M]//Production of Top 12 Biochemicals Selected by USDOE from Renewable Resources. Elsevier, 2022: 317-343. https://doi.org/10.1016/B978-0-12-823531-7.00014-7.

[27] Wang X, Li M, Wang M, et al. Thermodynamic analysis of glycerol dry reforming for hydrogen and synthesis gas production[J]. Fuel, 2009, 88(11): 2148-2153. https://doi.org/10.1016/j.fuel.2009.01.015.

[28] Nichele V, Signoretto M, Menegazzo F, et al. Glycerol steam reforming for hydrogen production: Design of Ni supported catalysts[J]. Applied Catalysis B: Environmental, 2012, 111: 225-232. https://doi.org/10.1016/j.apcatb.2011.10.003.

[29] Schwengber CA, Alves HJ, Schaffner RA, et al. Overview of glycerol reforming for hydrogen production[J]. Renewable and Sustainable Energy Reviews, 2016, 58: 259-266. https://doi.org/10.1016/j.rser.2015.12.279.

[30] Roslan NA, Abidin SZ, Ideris A, et al. A review on glycerol reforming processes over Ni-based catalyst for hydrogen and syngas productions[J]. International Journal of Hydrogen Energy, 2020, 45(36): 18466-18489. https://doi.org/10.1016/j.ijhydene.2019.08.211.

[31] Wilhelm DJ, Simbeck DR, Karp AD, et al. Syngas production for gas-to-liquids applications: technologies, issues and outlook[J]. Fuel processing technology, 2001, 71(1-3): 139-148. https://doi.org/10.1016/S0378-3820(01)00140-0.

[32] Dos Santos RG, Alencar AC. Biomass-derived syngas production via gasification process and its catalytic conversion into fuels by Fischer Tropsch synthesis: A review[J]. International Journal of Hydrogen Energy, 2020, 45(36): 18114-18132. https://doi.org/10.1016/j.ijhydene.2019.07.133.

[33] Ni M, Leung MKH, Leung DYC. Parametric study of solid oxide fuel cell performance[J]. Energy Conversion and Management, 2007, 48(5): 1525-1535.

https://doi.org/10.1016/j.enconman.2006.11.016.

[34] Xu HR, Chen B, Irvine J, et al. Modeling of CH4-assisted SOEC for H2O/CO2 co-electrolysis[J]. International Journal of Hydrogen Energy, 2016, 41(47): 21839-21849. https://doi.org/10.1016/j.ijhydene.2016.10.026.

[35] Wang C, He QJ, Li Z, et al. Modelling of solid oxide fuel cells with internal glycerol steam reforming[J]. International Journal of Hydrogen Energy, 2022, 47(33): 15012-15023. https://doi.org/10.1016/j.ijhydene.2022.03.001.

[36] Wang C, Li Z, Zhao SY, et al. Modelling of an integrated protonic ceramic electrolyzer cell (PCEC) for methanol synthesis[J]. Journal of Power Sources, 2023, 559: 232667. https://doi.org/10.1016/j.jpowsour.2023.232667.

[37] Rönsch S, Schneider J, Matthischke S, et al. Review on methanation–From fundamentals to current projects[J]. Fuel, 2016, 166: 276-296. https://doi.org/10.1016/j.fuel.2015.10.111.

[38] Li W, Wang H, Shi Y, et al. Performance and methane production characteristics of H2O–CO2 co-electrolysis in solid oxide electrolysis cells[J]. International Journal of Hydrogen Energy, 2013, 38(25): 11104-11109. https://doi.org/10.1016/j.ijhydene.2013.01.008.

[39] Wang Y, Zhu S, Lu J, et al. Boosting hydrogen production from steam reforming of glycerol via constructing moderate metal-support interaction in Ni@ Al2O3 catalyst[J]. Fuel, 2022, 324: 124583. https://doi.org/10.1016/j.fuel.2022.124583.

[40] Cheng CK, Foo SY, Adesina AA. Glycerol steam reforming over bimetallic Co–Ni/Al2O3[J]. Industrial & Engineering Chemistry Research, 2010, 49(21): 10804-10817. https://doi.org/10.1021/ie100462t.

[41] Stempien JP, Liu Q, Ni M, et al. Physical principles for the calculation of equilibrium potential for co-electrolysis of steam and carbon dioxide in a Solid Oxide Electrolyzer Cell (SOEC)[J]. Electrochimica Acta, 2014, 147: 490-497. https://doi.org/10.1016/j.electacta.2014.09.144.

[42] Suwanwarangkul R, Croiset E, Fowler MW, et al. Performance comparison of Fick's, dusty-gas and Stefan–Maxwell models to predict the concentration overpotential of a SOFC anode[J]. Journal of Power Sources, 2003, 122(1): 9-18. https://doi.org/10.1016/S0378-7753(02)00724-3.

[43] Veldsink JW, Van Damme RMJ, Versteeg GF, et al. The use of the dusty-gas model for the description of mass transport with chemical reaction in porous media[J]. Chemical Engineering Journal-Including Biochemical Engineering Journal, 1995, 57(2): 115-126. https://doi.org/10.1016/0923-0467(94)02929-6.

[44] Coker AK. Ludwig's applied process design for chemical and petrochemical plants[M]. gulf professional publishing, Houston, Texas, 2014. https://doi.org/10.1016/C2009-0-27075-9.

[45] Liu QG, Ma LX, Liu J. Handbook of Chemistry and Chemical Properties Data (Organic Volume) [M]. Chemical Industry Press, Beijing, 2002.

[46] Todd B, Young JB. Thermodynamic and transport properties of gases for use in solid oxide fuel cell modelling[J]. Journal of power Sources, 2002, 110(1): 186-200. https://doi.org/10.1016/S0378-7753(02)00277-X.

[47] Poling BE, Prausnitz JM, O'Connell JP, et al. The properties of gases and liquids[M]. vol. 12. Mcgraw-hill New York; 2001. https://doi.org/10.1063/1.3060771.

[48] Fuller EN, Ensley K, Giddings JC. Diffusion of halogenated hydrocarbons in helium. The effect of structure on collision cross sections[J]. The Journal of Physical Chemistry, 1969, 73(11): 3679-3685. https://doi.org/10.1021/j100845a020.

[49] Wang C, Li Z, He QJ, et al. Effect of Interconnector Rib on Optimization of SOFC Structural Parameters[J]. Journal of The Electrochemical Society, 2022, 169(9): 094511. https://doi.org/10.1149/1945-7111/ac911d.

[50] Lin CK, Chen TT, Chyou YP, et al. Thermal stress analysis of a planar SOFC stack[J].

Journal of Power Sources, 2007, 164(1): 238-251. https://doi.org/10.1016/j.jpowsour.2006.10.089.

[51] Liu XH, Zhou SH, Yan ZL, et al. Correlation between microstructures and macroscopic properties of nickel/yttria-stabilized zirconia (Ni-YSZ) anodes: Meso-scale modeling and deep learning with convolutional neural networks[J]. Energy and AI, 2022, 7: 100122. https://doi.org/10.1016/j.egyai.2021.100122.

[52] Ni M. An electrochemical model for syngas production by co-electrolysis of H2O and CO2[J]. Journal of power sources, 2012, 202: 209-216. https://doi.org/10.1016/j.jpowsour.2011.11.080.